Understanding the Impact of Different Types of Surface States on Photoelectrochemical Water Oxidation: A Microkinetic Modeling Approach

Kiran George,[1] *Tigran Khachatrjan,*[2] *Matthijs van Berkel,*[3,4] *Vivek Sinha,*[1,5] *and Anja Bieberle-Hütter*[1,*]

[1] Dutch Institute for Fundamental Energy Research (DIFFER), Electrochemical Materials and Interfaces, PO Box 6336, 5600 HH Eindhoven, The Netherlands.

[2] Eindhoven University of Technology, Department of Applied Physics, PO Box 513, 5600 MB Eindhoven, The Netherlands

[3] Dutch Institute for Fundamental Energy Research (DIFFER), Energy Systems & Control, PO Box 6336, 5600 HH Eindhoven, The Netherlands

Abstract

Oxygen evolution reaction (OER) has been identified as one of the performance-limiting processes in solar water splitting using photoelectrochemical (PEC) cells. One of the reasons for the low OER performance is related to the existence of different types of surface states at the semiconductor-electrolyte interface: recombining surface states (r-SS) and surface states due to intermediate species (i-SS). Since the impact of surface states on OER is still under debate, we investigate how different types of surface states affect PEC water oxidation and how they impact experimental measurements. In a new computational approach, we combine a microkinetic model of the OER on the semiconductor surface with the charge carrier dynamics within the semiconductor. The impact of r-SS and i-SS on the current-voltage curves, hole flux, surface state capacitance, Mott-Schottky plots, and chopped light measurements are systematically investigated. It is found that a) r-SS results in a capacitance peak below the OER onset potential, while i-SS results in a capacitance peak around the onset potential; b) r-SS leads to an increase in OER onset potential and a decrease in saturation current density; c) r-SS leads to Fermi level pinning before the onset potential, while i-SS does not result in Fermi level pinning; d) a smaller capacitance peak of i-SS can be an indication of lower catalytic performance of the semiconductor surface. Our approach in combination with experimental comparison allows distinguishing the impact of r-SS and i-SS in PEC experiments. We conclude that r-SS reduces OER performance and i-SS mediates OER.

KEYWORDS

Oxygen evolution reaction, photoelectrochemical cell, surface states, Fermi level pinning, semiconductor-electrolyte interface.

1 Introduction

Water splitting using sunlight is a promising path for storing solar energy in chemical bonds and thereby producing ‘solar fuels’.[1] A potential cost-effective method to produce solar fuels is by using a photoelectrochemical (PEC) cell.[2] In a PEC cell, hydrogen is generated at the cathode, and oxygen is generated at the anode.[3] The half-reactions are called hydrogen evolution reaction (HER) and oxygen evolution reaction (OER), respectively. Among the two half-reactions, OER accounts for most of the overpotential required for water splitting and is found to be the performance limiting reaction in PEC water splitting.[4,5] Hence, current research focuses on improving OER and thereby improving the efficiency of PEC water splitting.[6–8] The photoanode of a PEC is typically made of a semiconductor with a suitable bandgap which provides the thermodynamic potential required for water splitting.[9] Fe_2O_3, TiO_2, WO_3, and $BiVO_4$ are some of the metal oxide photoanode materials that are studied in the literature.[10–15] However, the efficiencies of the PEC photoanodes using these materials are not high enough for commercialization of PEC yet.[2]

Among the different photoanode materials, Fe_2O_3 (hematite) is studied extensively in the literature due to its stability, abundance, low cost, and non-toxicity.[9,16] Theoretically, a PEC cell with a hematite photoanode can achieve a solar to hydrogen conversion efficiency of around 15.5%; however, practically reported efficiencies are much lower.[16,17] One of the reasons for this lower performance compared to theoretical prediction is attributed to the existence of mid-band gap energy states, so-called surface states.[7,18] In the literature, two types of surface states are reported in photoanodes. The first type is related to defects at the surface of the semiconductor, such as vacancies or dangling bonds, which result in the recombination of charge carriers.[3] This type of surface state is referred to as 'recombining surface state (r-SS)'.[19–21] The second type is due to the presence of adsorbed species on the surface. Such surface states are observed only during water oxidation and are absent when a hole scavenger is added to the electrolyte.[22] These surface states are assumed to be the surface intermediates that are formed during OER. They are referred to as 'surface states due to OER intermediates (i-SS)'.[19–21] These surface states play an important role in the performance of photoanodes, and hence, a thorough understanding of the function and impact of surface states is necessary .[20]

When a potential is applied across an interface having surface states, a fraction of the applied potential is lost in the charging of the surface states.[23] The potential range in which the surface states are getting charged, band bending of the semiconductor does not occur; hence, the Fermi level remains pinned.[24] Fermi level pinning (FLP) is usually identified from Mott-Schottky analysis.[25,26] FLP and the potential over which the surface state charging occurs, is seen in Mott-Schottky analysis as a plateau region.

FLP due to both r-SS and i-SS has been reported in the literature. For example, Zandi et al.[7,25] have reported FLP at applied potentials lower than the onset potential for Fe_2O_3. After selective removal of deleterious surface states (in this context, r-SS) using controlled annealing of the electrode, the FLP was no longer visible in the Mott-Schottky plot.[7,25] Similar studies have identified such FLP at applied potentials lower than the onset potential.[27] In the case of i-SS, Klahr et al.[22] identified FLP occurring around the OER onset potential. From the electrochemical impedance spectroscopy measurements, a capacitance was observed around the same potential range. This capacitance was seen only during water oxidation and was absent during measurements with a hole scavenger.[22] Hence, the capacitance and FLP was attributed to i-SS. In a similar study, positive shifts in the Mott-Schottky plots were observed with an increase in illumination intensities and were associated with FLP due to the charging of i-SS.[26] Based on these observations, it is believed that i-SS leads to FLP around the OER onset potential.

Thus, the existence of two distinct types of surface states has been pointed out in the literature.[7] However, the impact of these surface states on the performance of OER is still debated.[28,29] One of the most accepted explanations is that the surface states reduce the overall performance of OER.[22,27] On the contrary, some studies suggest that the surface states mediate OER.[21,26,30] In a recent experimental study, Shavorskiy et al.[31] proposed that surface states do not play a major role in mediating OER. Conclusively, these different views suggest that the role of surface states is still a topic of debate in the field of PEC.

From experimental observations, it is challenging to pinpoint the individual and combined impact of surface states on the efficiency of OER. Particularly, the impact of i-SS on the performance of OER is difficult to analyze. Despite some promising operando studies, experimental data regarding the impact of OER intermediates are still largely absent due to experimental challenges associated with the identification of OER intermediates.[30,32] However, using modeling and simulations clear insights about each of these surface states can be obtained by analyzing the sensitivity of measurements to the model parameters associated with each surface state.

The goal of our study is to pinpoint the impact of r-SS and i-SS on PEC data, such as j-V curves, surface state capacitance, Mott-Schottky plots, hole flux, and chopped light measurements. To analyze the impact of i-SS on the PEC data, it is important to include the elementary steps in OER and the adsorbed OER intermediates in the model. The charge transferred in the formation of the adsorbed OER intermediates is analogous to charge carriers getting trapped at the surface. Previously, we developed a microkinetic model of OER specifically for semiconductor electrodes.[33] In the current paper, we add illumination and charge carrier dynamics to the same framework of the microkinetic model of OER. For simulating r-SS, a monoenergetic state with energy E_T and density N_T (T stands for 'trap') is assumed within the bandgap of the semiconductor.[34] Thus, we present in this paper an extended model to George et al.[33] which brings together the elementary steps in OER and charge carrier dynamics within the semiconductor. Modeling of charge carrier dynamics has been done before in the literature.[35,36] However, the charge carrier dynamics has so far not been coupled to the multistep mechanism of OER at the interface.

The impact of the presence of r-SS and i-SS on electrochemical data is pointed out based on the simulated data. The presence of r-SS results in an increase in the onset potential and reduces the saturation photocurrent density. We show a direct relationship between the coverage of OER intermediates and capacitance due to i-SS. From the Mott-Schottky analysis, we find that the capacitance due to i-SS does not necessarily result in the FLP observed around the onset potential as reported in the literature. On the contrary, the FLP observed in experiments around the onset potential is found to be related to the IR drop over series resistance which drastically increases around the onset potential. The approach presented in this work shows how a model combining multiple steps in OER and charge carrier dynamics contributes to a clear understanding of the impact of surface states on typical PEC data.

2 Theory and method

As the OER involves the transfer of four charge carriers, it is proposed that the OER proceeds through four intermediate steps, each step involving the transfer of a single charge carrier.[37,38] In the literature, different mechanisms have been proposed for the electrochemical mechanism of OER.[38–40] Previously, in George et al.[33], we have simulated the hematite-electrolyte interface using a microkinetic model of OER based on the four-step electrochemical mechanism of OER on the semiconductor surface.[33] The model related PEC data, such as current density and electrochemical impedance spectra to the kinetics of elementary reactions in OER. The charge carrier density at the surface was simplified as an exponential function of applied potential. In this work, we extend this microkinetic model of OER by adding the charge carrier dynamics explicitly. The general approach adopted in the modeling is summarized in Figure 1. The input-output relationship is similar to that of experiments: applied potential (V_{applied}) and illumination intensity (I_0) are the input to the model and current density (j) is the output.

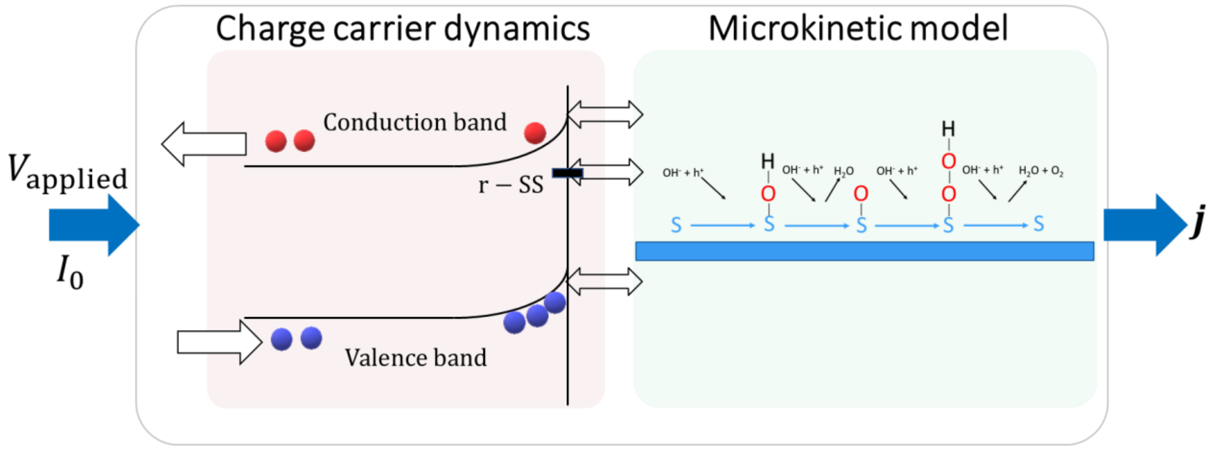

Figure 1 General approach for simulating the hematite-electrolyte interface: coupling of a microkinetic model with the charge carrier dynamics within the semiconductor; applied potential ($V_{applied}$) and illumination intensity (I_0) are the input to the model and current density (j) is the output.

For ideal semiconductor electrodes, OER can occur by charge transfer via the valence band (VB) and/or the conduction band (CB).[41] For experimental semiconductor electrodes, the literature has reported about intrinsic mid-band gap states or r-SS at the semiconductor-electrolyte interface (SEI).[42] The r-SS is defined in our model as a monoenergetic state at an energy level of E_{T} within the bandgap with a surface state density denoted by N_{T}.[34] All the charge transfer pathways, namely via VB, CB, and r-SS are considered for OER to occur and are denoted by the three double-sided arrows in Figure 1. The probability of OER occurring via VB, CB, and r-SS depends on the kinetics of the multiple steps in OER and the charge carrier concentrations at each of these bands. In the approach shown in Figure 1, the microkinetic model considers the kinetics of the multiple steps in OER; the charge carrier concentration is calculated by modeling the charge carrier dynamics within the semiconductor.

2.1 Microkinetic Model

We have previously developed a microkinetic model of OER specifically for semiconductor electrodes.[33] To give a quick review, the microkinetic model was developed based on the multistep mechanism of OER proposed by Rossmeisl et al.[38] This mechanism involves OH, O, OOH, and O_2 as the adsorbed intermediates.[38,43] Based on the multiple steps in OER, the rate of formation of the adsorbed OER intermediates is written as a set of ordinary differential equations. Solving this set of differential equation for a single site on the semiconductor surface gives the fractional coverage of each OER intermediate, represented as $\theta_{\mathrm{OH}}, \theta_{\mathrm{O}}, \theta_{\mathrm{OOH}}$, and $\theta_{\mathrm{O_2}}$. The charge transfer in this model was assumed to occur via the VB. The rate constant for charge transfer via VB is calculated using Gerischer theory for semiconductors.[41,44] Based on the charge transferred across the interface during the multistep reactions, the current density due to the reaction is calculated. More details about the model can be found in George et al.[33]

In this paper, we use the same approach for calculating the fractional coverage of OER intermediates and the current density due to the reactions. The electrochemical mechanism of OER under alkaline pH is used for developing the microkinetic model (supporting information S1.1). The rate of formation of OER intermediates is calculated assuming charge transfer via VB, CB, and r-SS. As mentioned earlier, the presence of r-SS is a deviation from the ideal surface of the photoanode. For this reason, the sites associated with r-SS (henceforth denoted as r-SS sites) are different from those of the sites on the ideal photoanode surface (henceforth denoted as ideal sites). In the model, the OER at r-SS sites and ideal sites are treated separately and the intermediate species adsorbed at r-SS sites are assumed to not interact with OER intermediate at the ideal adsorption sites. The OER occurring at the ideal sites involve charge transfer via VB and CB as in the case of an ideal semiconductor. In the case of OER at r-SS sites, the charge transfer occurs only via r-SS.

The rate of formation of OER intermediates at the ideal site and the rate constants for charge transfer via VB and CB are given in the supporting information S1.2. The rate constants are defined based on the Gerischer model of charge transfer.[41] The rate equations for OER at r-SS sites and the rate constant for charge transfer via r-SS can be calculated similarly to that of the VB and CB as given in the supporting information S1.3.

By solving the rate equations, the fractional coverage of the four OER intermediates at the ideal sites can be calculated ($\theta_{\mathrm{OH}}, \theta_{\mathrm{O}}, \theta_{\mathrm{OOH}},$ and $\theta_{\mathrm{O_2}}$). Similarly, the fractional coverage of OER intermediates at r-SS sites, denoted by $\theta T_{\mathrm{OH}}, \theta T_{\mathrm{O}}, \theta T_{\mathrm{OOH}},$ and $\theta T_{\mathrm{O_2}}$, can be obtained by the solution of the set of equations in S1.3. For solving the rate equations, it is necessary to input the charge carrier concentrations at each energy band, which depends on the charge carrier dynamics within the semiconductor.

2.2 Charge carrier dynamics

The processes that belong to the charge carrier dynamics within the semiconductor are illustrated in Figure 2. Under illumination (I_0), electrons (red circles) in the semiconductor are excited from the valence band to the conduction band leaving holes (blue circles) in the valence band. Under an applied potential (V_{applied}), the electrons move towards the back contact and holes move towards the semiconductor-electrolyte interface (SEI). Some of these holes recombine directly with the electrons and some of the holes can get trapped at r-SS where they recombine with electrons from the conduction band. In Figure 2, k_{rec} represents the rate of direct recombination of holes and electrons in the space charge region,[45] k_{p} represents the rate at which holes get trapped in r-SS, and k_{n} represents the rate at which electrons recombine with holes in r-SS. As mentioned in the previous section, the charge carriers at the surface take part in OER via VB, CB, and r-SS. The rate constants $K_{\mathrm{vf,b}}$, $K_{\mathrm{cf,b}}$ and $K_{\mathrm{tf,b}}$ represent the forward and backward rate constants for charge transfer via VB, CB, and r-SS, respectively. The rate at which charge transfer occurs via VB, CB, and r-SS can affect the carrier concentrations at respective energy levels. The cumulative effect of all these processes determines the charge carrier concentrations at the surface. In this section, we calculate the concentration of holes at the surface (p_s), the concentration of electrons at the surface (n_s), and the fill factor of electrons (f_T) in r-SS.

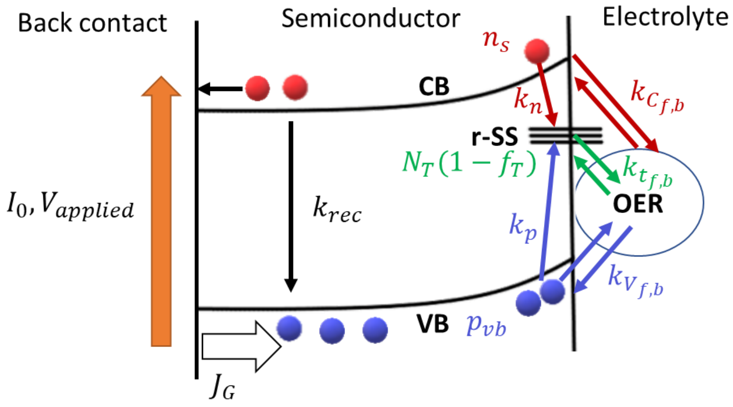

Figure 2 Schematic of charge carrier dynamics under illumination within the space charge region showing recombination, trapping, and oxygen evolution reaction via VB (blue), CB (red), and r-SS (green). The red circles represent electrons and the blue circles represent holes.

The flux of holes (J_G) to the surface for an illumination intensity of I_0 is given by the Gartner equation as[46]

$$J_G = I_0\left(1 - \frac{\exp(-\alpha W_{sc})}{1 + \alpha L_p}\right) \tag{1}$$

where α represents the absorption coefficient at a given wavelength, W_{sc} the width of the space charge region, and L_p the minority carrier diffusion length. The width of the space charge region is related to the potential across the space charge region (u_{sc}) given by[3]

$$W_{sc} = \sqrt{\frac{2\epsilon_r\epsilon_0}{eN_D}(u_{sc} - k_B T/e)} \tag{2}$$

where ϵ_r is the permittivity of the semiconductor material, ϵ_0 is the permittivity of free space, N_D is the doping density, e is the charge of an electron, k_B is the Boltzmann constant, and T is the temperature.

The applied potential ($V_{applied}$) in the model is defined similar to experiments, in terms of scan rate (Sr), i.e. $V_{applied} = Sr \cdot time$.

For n-type materials, electrons are the majority carriers and the electron concentration at the surface under illumination (n_{s}) can be approximated as an exponential function of the potential across the space charge region given by[47]

$$n_{\mathrm{s}} = n_{\mathrm{s}0}\, exp\left(-\frac{u_{\mathrm{sc}}}{(k_{\mathrm{B}}T/e)}\right) \tag{3}$$

where n_{s0} represents the concentration of surface electrons in the dark under zero bias.

The rate of change of hole density at the semiconductor surface (p_s) depends on several factors and can be calculated as follows[35,47]

$$\frac{dp_{\mathrm{s}}}{dt} = \frac{J_{\mathrm{G}}}{d} + \left(\frac{Sr}{k_{\mathrm{B}}T/e}\right) p_{\mathrm{s}0} \exp\left(\frac{u_{\mathrm{sc}}}{k_{\mathrm{B}}T/e}\right) - k_{\mathrm{rec}} n_{\mathrm{s}} p_{\mathrm{s}} - \frac{N_{\mathrm{T}}}{d} k_{\mathrm{p}} p_{\mathrm{s}} f_{\mathrm{T}} - \frac{N_0}{d}\sum_{\mathrm{i}=1}^{4}\left(\left(K_{\mathrm{v}_{\mathrm{f,i}}}\theta_{\mathrm{red,i}} - K_{\mathrm{v}_{\mathrm{b,i}}}\theta_{\mathrm{ox,i}}\right) + \left(K_{c_{\mathrm{f,i}}}\theta_{\mathrm{red,i}} - K_{c_{\mathrm{b,i}}}\theta_{\mathrm{ox,i}}\right)\right) \tag{4}$$

The first term represents the hole flux under applied potential and illumination (J_{G}). The term d is the thickness of the hole accumulation layer and is used to convert the surface concentration of holes (per cm^2) to volume concentration (per cm^3).[23] The second term is the potential-dependent dark current where p_{s0} represents the concentration of surface holes in the dark under zero bias. The third and fourth terms represent the rates at which holes recombine directly ($k_{\mathrm{rec}} n_s p_s$) and get trapped at r-SS ($k_{\mathrm{p}} p_{\mathrm{s}} N_{\mathrm{T}} f_{\mathrm{T}}/d$).[47] The last term in Eq. (4) represents the rate at which holes are consumed in OER via the ideal adsorption sites. N_0 represents the total number of ideal adsorption sites on the semiconductor surface. The summation Σ over i = 1 to 4 denotes that all four steps in OER (microkinetic equations) are taken into account for the calculation of the charge carrier concentration. The concentration of reduced and oxidized OER intermediates at the sites are represented as $\theta_{\mathrm{red,i}}$ and $\theta_{\mathrm{ox,i}}$.

The holes reach the traps at a rate of k_p. These holes can recombine with the electrons from the conduction band at a rate of k_n or they can participate in OER with a rate of K_t.[35] The overall effect of these processes at r-SS changes its fill factor of electrons which is denoted by f_T. The rate of change of electron density in r-SS can be calculated as[35,47]

$$N_{\mathrm{T}} \frac{df_{\mathrm{T}}}{dt} = k_{\mathrm{n}} n_{\mathrm{s}} N_T (1 - f_{\mathrm{T}}) - k_{\mathrm{p}} p_{\mathrm{s}} N_{\mathrm{T}} f_{\mathrm{T}} + N_{\mathrm{T}} \sum_{i=1}^{4} (K_{\mathrm{t_{f,i}}} \theta T_{\mathrm{red,i}} - K_{\mathrm{t_{b,i}}} \theta T_{\mathrm{ox,i}}) \tag{5}$$

The last summation term in Eq. (5) is similar to that in Eq. (4) and represents the rate at which holes are consumed for OER via r-SS. This increases the electron density in r-SS and, hence, the last term has a positive sign. $\theta T_{\mathrm{red,i}}$ and $\theta T_{\mathrm{ox,i}}$ represent the fractional concentrations of OER intermediates at r-SS sites.

The effect of OER intermediates on the charge carrier dynamics is defined in the model through the last terms in Eq. (4) and Eq. (5). From Eq. (3)-(5), it can be seen that there are two main input variables similar to experiments, the illumination intensity which enters through J_{G} and the applied potential which enters through u_{sc} and Sr. The value I_0 is a constant based on the illumination intensity. The potential across the space charge region (u_{sc}) is different from the applied potential and its calculation is discussed in the next section.

2.3 Potential across the space charge region

The potential across the space charge region (u_{sc}) is required for the calculation of the Gartner hole flux (Eq. (1)-(2)), the electron density (Eq. (3)), and the hole density in the dark (second term in Eq. (4)). The potential across the space charge region is defined as[48,49]

$$u_{\mathrm{sc}} = V_{\mathrm{applied}} - V_{\mathrm{fb}} - V_{\mathrm{H}} - V_{\mathrm{IR}} \tag{6}$$

where V_{applied} is the applied potential. V_{fb} is the flat band potential; it depends on the material of the electrode, the treatment of the electrode, and experimental conditions.[50] V_{fb} is assumed to be constant in the simulations. V_{H} is the potential across the Helmholtz layer which can be calculated based on the fill factor and surface state density of r-SS as given by Memming et al.[47]

$$V_{\mathrm{H}} = \frac{eN_{\mathrm{T}}(1 - f_{\mathrm{T}})}{C_{\mathrm{H}}} \tag{7}$$

where C_{H} is the Helmholtz capacitance. C_{H} is assumed to be constant.[51] The potential drop across the Helmholtz layer results in an equivalent shifting of the valence and conduction band energy levels (E_{V} and E_{C}) which is considered in the calculation of the rate constants (supporting information S1.2 and S1.3). [47]

The last term in Eq. (6) represents the IR drop over the series resistance (R_{s}). Klotz et al.[52] have shown that it is necessary to include series resistance in models aimed at explaining photoelectrochemical experiments. The series resistance in a PEC is related to the back contact resistance and the interfacial and bulk resistances of the electrolyte.[52–54] The IR drop over R_{s} is given by[55]

$$V_{\mathrm{IR}} = j \cdot R_{\mathrm{s}} \tag{8}$$

Thus, the IR drop over the series resistance is directly proportional to the current in the system at that operating point. R_{s} is usually one or two orders of magnitude lower compared to the other ohmic contributions in typical equivalent circuit model elements of PEC and is usually considered negligible. However, from the literature, it is found that certain electrode treatments like high-temperature annealing also result in a substantial increase in R_{s}.[56,57] Hence, it is important to include the potential drop across R_{s}. The implementation of the IR drop in the model is represented as a schematic in Figure S1 of the supporting information.

2.4 Current density

The current density related to OER depends on the intermediate reactions which occur due to charge transfer via VB, CB, and r-SS. By simultaneously solving the microkinetic rate equations for OER intermediates (supporting information: Eq. S.15 -S.19 and Eq. S.30-S.34) along with Eq. (3)-(5), the fractional coverage of OER intermediates and charge carrier densities can be calculated for any given scan rate and illumination intensity. Using these calculated quantities, the current due to reactions via VB, CB, and r-SS ($j_\mathrm{v}, j_\mathrm{c}, j_\mathrm{t}$) is calculated (supporting info Eq. S.22, S.25, S.37). The sum of all these currents gives the current density related to OER as

$$j = j_\mathrm{v} + j_\mathrm{c} + j_\mathrm{t} \tag{9}$$

The current density associated with the hole flux is called the hole current density (j_h) and is calculated as [58]

$$j_\mathrm{h} = e \cdot J_\mathrm{G} \tag{10}$$

where J_G is the hole flux from Eq. (1).

2.5 Capacitances

The model considers several capacitances. The Helmholtz capacitance is an input to the model (Eq. (7)); it is assumed to be a constant. The capacitances related to r-SS, i-SS, and the capacitance of the space charge region are capacitances which are calculated in post-processing.

The capacitance due to r-SS ($C_\mathrm{r-SS}$) is calculated as[34,59]

$$C_\mathrm{r-SS} = e^2 N_\mathrm{T} f_\mathrm{T}(1 - f_\mathrm{T})/k_\mathrm{B}T \tag{11}$$

According to the mechanism of OER, as given in the supporting information S1.1, the formation of intermediate species at the interface means that holes are locked up on the surface. The fractional coverage of the OER intermediates at the surface of the photoanode (Eq. S15-Eq. S19) can be calculated using the model for any given input conditions.

The capacitance due to i-SS ($C_\mathrm{i-SS}$) is calculated, based on the standard definition of capacitance ($C = dq/dV$), as the rate of change of charge accumulated in the formation of OER intermediates with respect to the change in applied potential.[20] Hence, for a fractional coverage of all adsorbed surface species θ_ad and for the total number of adsorption sites N_0, the total charge accumulated at the surface can be calculated as $N_0 \cdot e \cdot \theta_\mathrm{ad}$. Here, e represents the charge of an electron. The capacitance due to i-SS is thus calculated as

$$C_{\text{i-SS}} = \frac{dq_{\text{i-SS}}}{dV} = N_0 \cdot e \cdot \frac{d\theta_{\text{ad}}}{dV} = \frac{N_0 e\left(d\theta_{\text{OH}} + d\theta_{\text{O}} + d\theta_{\text{OOH}} + d\theta_{\text{O}_2}\right)}{dV} \tag{12}$$

The capacitance of the space charge region (C_{sc}) is calculated using the Mott-Schottky relation[3]

$$(1/C_{\text{sc}})^2 = (2/\epsilon_{\text{r}}\epsilon_0 e N_{\text{D}} A^2)(u_{\text{sc}} - k_{\text{B}}T/e) \tag{13}$$

where N_{D} is the doping density and A is the area of the electrode.

The model is implemented in MATLAB® and the set of differential equations is solved using a stiff ODE-solver, 'ode15s', in MATLAB®.[60]

3 Results and discussion

The model discussed in section 2 is generic and can be used for simulating PEC characteristics for any semiconductor photoanode by substituting material-specific constants. For the simulations in this paper, we chose hematite (α-Fe_2O_3) as the model system. The Gibbs free energy changes (ΔG_{i}) for the OER intermediate reactions on hematite (110) surface are calculated using DFT (supporting information S2) and are given in Table S2.[61] The redox potential of each intermediate step $\left(E_{\text{redox,i}}\right)$ can be calculated using the standard relation between Gibb's free energy and redox potential.[33] These redox potentials are substituted in the Gerischer equation for calculating the rate constants for the multistep reactions.[33] The calculation of rate constants is described in George et al.[33] and the supporting information S1.2 and S1.3. The parameters used for the simulations in this paper are given in Table 1.

Table 1 Model parameters, their descriptions, and values used in the simulations.

Parameter	Description	Value	Reference
E_{V}	Val. band energy level for hematite	2.4	[17]
E_{C}	Cond. band energy level for hematite	0.3	[17]
E_{T}	Trap state energy level	E_{C} + 0.4	

n_{s0}	Electron density under zero bias	N_{D}	
p_{s0}	Hole density in the dark under zero bias	1 cm^{-3}	
R_{s}	Series resistance	30 $\Omega \cdot \mathrm{cm}^2$	
α	Absorption coefficient	1.5 x 10^5 cm^{-1}	23
L_{p}	Hole diffusion length	4 x 10^{-7} cm	62
ϵ_{r}	Relative permittivity of hematite	38	63
V_{fb}	Flat band potential	0.4 V	63
I_0	Illumination intensity	1 x 10^{16} cm^2	23
σ_{p}	Electron capture cross section of holes	1 x 10^{-16} cm^2	23
v_{th}	Thermal velocity of electrons	1 x 10^5 cm/s	23
$k_{\mathrm{n}}, k_{\mathrm{p}}$	Electron and hole trapping rates	$\sigma_{\mathrm{p}} \cdot v_{\mathrm{th}}$ (cm^3/s)	23
k_{rec}	Direct recombination rate within SCR	1 x 10^{-6} cm^3/s	
d	Thickness of hole accumulation layer	1 x 10^{-7} cm	23,34
C_{H}	Helmholtz capacitance	20 x 10^{-6} F/ cm^2	51
N_{D}	Doping density	3 x 10^{18} cm^{-3}	63
$N_{0,\mathrm{ideal}}$	No. of ads. sites on ideal hematite surface	2.9 x 10^{14} cm^{-2}	20
N_{T}	Surface state density of r-SS	1 x 10^{13} cm^{-2}	
N_0	No. of ads. sites on the surface in the presence of r-SS	$N_{0,\mathrm{ideal}} - N_{\mathrm{T}}$;	

Additional constants used in the simulation associated with the microkinetic model are given in the supporting information in Table S1.

3.1 Validation of input-output relationship

For comparability with experiments, the model is developed such that it holds the same input-output relationship as experiments with applied voltage and illumination intensity as the input and current density as the output. To validate the input-output relation of the model, we simulate current densities as a function of applied potential at different illumination intensities as shown in Figure 3.

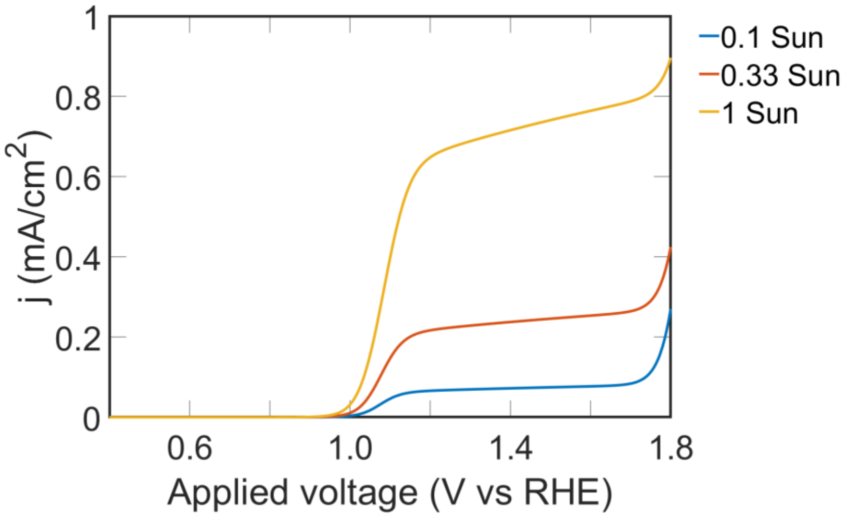

Figure 3 Simulated j-V plots under different illumination intensities. The current density changes as a function of applied potential and illumination intensity showing qualitative agreement with PEC measurements, such as shown for example in.[26] The onset potential is around 0.9 V vs. RHE and the saturation current density increases with an increase in illumination intensity.

The simulated j-V curves have onset potentials around 0.9 V vs. RHE. The sharp increase in current density around 1.7 V vs. RHE is related to the increase in dark current at high potentials. It is found that the saturation current density increases with an increase in illumination intensity. The input-output relationship observed in Figure 3 is in good qualitative agreement with experimental data from the literature.[26] Experimental j-V plots for three different illumination intensities for hematite electrodes are shown in the supporting information in Figure S2.[26] Thus, the developed model can qualitatively simulate current density data similar to the experiments for given applied potentials and illumination intensities.

3.2 The impact of r-SS

In this section, we investigate the impact of r-SS on the electrochemical data, in particular on the j-V curves, surface state capacitance, Mott-Schottky data, and the hole flux. The characteristics of r-SS are defined by its energy level (E_T), surface state density (N_T), and the trapping rates ($k_\mathrm{n}, k_\mathrm{p}$). A typical value of 0.4 eV below the conduction band is used for E_T of r-SS based on the literature.[31] The N_T of these sub-conduction band states in PEC electrodes usually varies between 10^{12} to $10^{14}\mathrm{cm}^{-2}$.[64,65] We use three different values for N_T in the simulations, i.e. $5 \cdot 10^{12}\mathrm{cm}^{-2}$, $1 \cdot 10^{13}\mathrm{cm}^{-2}$, and $2 \cdot 10^{13}\mathrm{cm}^{-2}$. The trapping rates ($k_\mathrm{n}, k_\mathrm{p}$) are calculated based on literature using the trapping cross-section and the thermal velocity of the charge carriers.[23] The trapping rates are assumed to be independent of N_T; the values are given in Table 1. An advantage of the simulations compared to experimental studies is that the N_T and E_T can be systematically changed and their impact on the PEC characteristics can be studied. In experiments, it is difficult to perform such investigations systematically and quantitatively, as often several parameters change at the same time.

The capacitance due to r-SS is calculated according to Eq. (11) and is plotted in Figure 4a as a function of applied potential. A bell-shaped curve is found for $C_\mathrm{r-SS}$. The bell-shape becomes wider, the maximum of $C_\mathrm{r-SS}$ increases, and the potential corresponding to the maximum increases with an increase in N_T. $C_\mathrm{r-SS}$ reaches maximum values of 10 µF/cm^2 to 30 µF/cm^2. These observations can be explained as follows: in the presence of r-SS and under an applied potential, the generated holes get trapped in the surface states until the surface states are completely filled. The magnitude of peak capacitance increases with N_T as more charge get accumulated with an increase in N_T. According to Eq. (11), the maximum capacitance occurs, when r-SS is half-filled ($f_\mathrm{T} = 0.5$). The higher the N_T, the higher the potential required for the filling of r-SS. Therefore, the potential corresponding to the maximum of $C_\mathrm{r-SS}$ increases and the capacitance peak broadens with higher N_T. For the same energy level of r-SS, i.e. E_T = 0.4

eV below the conduction band, the maxima of $C_{\mathrm{r-SS}}$ are located at different applied potential due to the change in N_{T}. This indicates that the applied potential corresponding to the maximum of $C_{\mathrm{r-SS}}$ cannot be used as a direct indication of the energy level of the surface state. The peak position depends on a combined effect of E_{T}, N_{T}, k_{n}, and k_{p}.

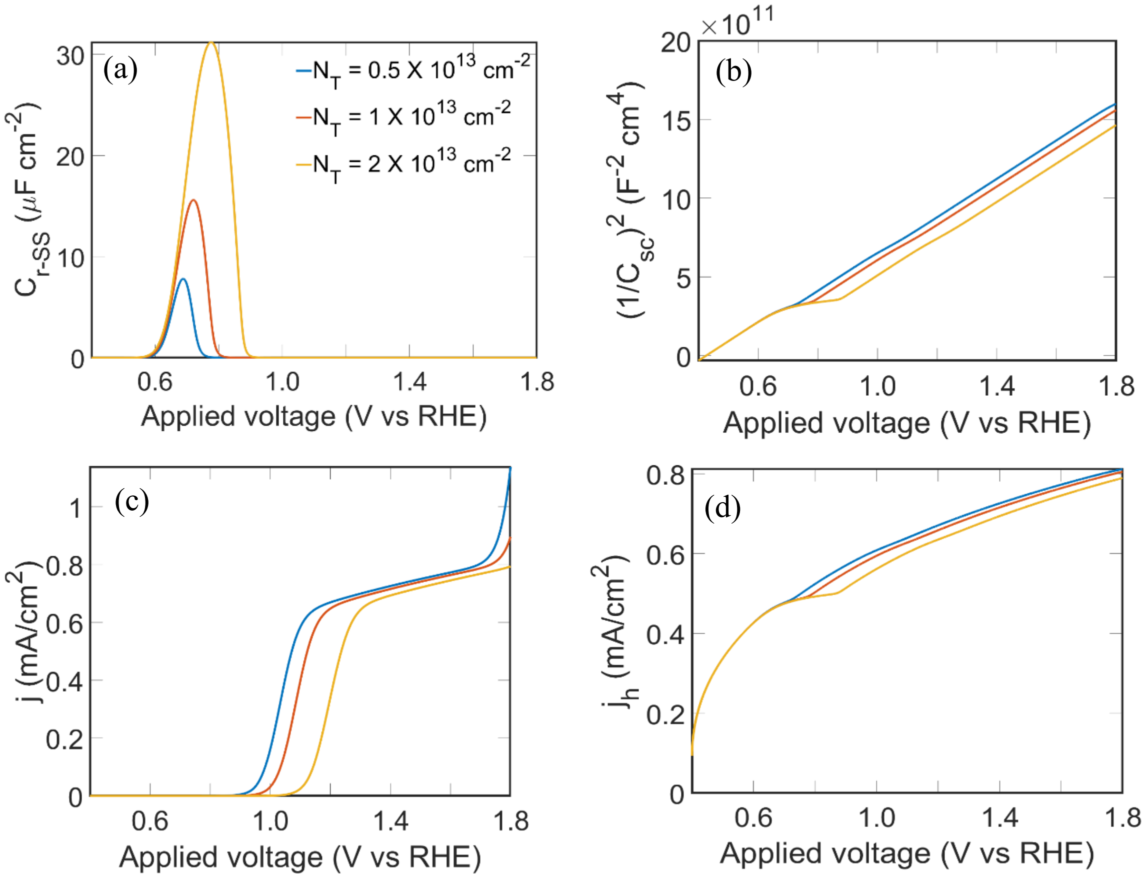

Figure 4 a) Effect of surface state density of r-SS (N_{T}) on a) the surface state capacitance, $C_{\mathrm{r-SS}}$, as a function of applied potential; both the maximum and the full width at half maximum of $C_{\mathrm{r-SS}}$ increase with an increase in N_{T}; b) the Mott-Schottky plots; the pinning coincide with $C_{\mathrm{r-SS}}$ and the FLP is extended when N_{T} is increased; c) the j-V plots; higher onset potential and lower saturation current density are found with higher N_T; and d) the hole current density (j_{h}); a plateau is observed before potentials corresponding to the onset potential from j-V plots and the plateau increases with an increase in N_{T}.

The impact of $C_{\mathrm{r-SS}}$ on the potential distribution within the space charge region is investigated using Mott-Schottky analysis. Figure 4b shows simulated Mott-Schottky plots for the same model parameters as in Figure 4a. A plateau is observed around an applied potential of 0.8 V vs. RHE; the plateau widens with an increase in N_{T}. According to the Mott-Schottky equation in Eq. (13), $(1/C_{\mathrm{sc}})^2$ is proportional to u_{sc} and, hence, the Mott-Schottky plot should be linear. Usually a plateau in the Mott-Schottky curve is associated with FLP.[3] Therefore, the plateau around 0.8 V vs. RHE indicates FLP due to r-SS as the potential range of the FLP coincides with the potential range of the maximum of $C_{\mathrm{r-SS}}$ in Figure 4a. This means that the potential across the space charge region decreases with an increase in N_{T}.

The simulated j-V curves are shown as a function of N_{T} in Figure 4c. The j-V curve shifts anodically with an increase in N_{T} which results in higher onset potential and lower saturation current density. This behavior is in agreement with experimental j-V curves from the literature showing lower onset potential when surface states are passivated.[7,66] The increase in N_{T} leads to a decrease in u_{sc} according to Eq. (6) and (7). Consequently, a higher potential has to be applied for OER to occur which explains the higher onset potential. The decrease in the saturation current with the increase in N_{T} is also related to the decrease in u_{sc} as it leads to a decrease in W_{sc} and the hole flux according to Eq. (1) and Eq. (2).

The impact of r-SS on the hole flux is analyzed in Figure 4d. The hole flux to the surface is calculated according to the Gartner equation (Eq. (1)) and the hole current density (j_{h}) is calculated using Eq. (10). j_{h} is simulated for three different N_{T} and is shown in Figure 4d. The simulated j_{h} shows that the magnitude of hole current at higher potentials decreases with an increase in N_{T}. This decrease in hole current at higher potentials explains the decrease in saturation current density in Figure 4c as the OER photocurrent at higher potentials matches with the hole current.[23,58] Additionally, in Figure 4d, the hole current shows a plateau before the potential corresponding to OER onset. It is found that the potential range of the plateau coincides with the potential range of the $C_{\mathrm{r-SS}}$ peaks. The presence of such a plateau is observed in experimental hole current density reported in the literature.[7,22] The relation between N_{T} and the plateau observed in hole current density is in agreement with the experimental data from Zandi and Hamann comparing samples before and after surface state removal.[7] In experiments, the hole current density is measured by adding hole scavengers, like H_2O_2 or $[Fe(CN)_6]^{3-/4-}$ in the electrolyte. Thus, we show that the existence of r-SS has an impact on the hole current density/hole flux and a flattening in the hole current density before the onset potential of photocurrent is an indication of the presence of r-SS.

As discussed in section 2.1, charge transfer via valence band, conduction band, and via r-SS is included in the model. Charge transfer may occur via these bands and results in OER depending on the corresponding charge transfer rate constants. In all the cases shown in Figure 4, OER occurs with charge transfer via valence band and conduction band. No charge transfer is observed to occur via r-SS as OER intermediates are not formed at the sites corresponding to r-SS with the assumed energy level, E_{T}, (0.4 eV below E_c). To check the sensitivity of the data towards the energy level of r-SS, simulations are run with three different E_{T} values: 0.3 eV, 0.4 eV, and 0.5 eV below E_{C}. The simulated data is insensitive to the variation of the energy level of r-SS in the tested range and with constant trapping rates. Based on the theory, there is a possibility for surface states with energies outside the bandgap.[67] However, as the energies of these surface states are not within the bandgap, they will not lead to Fermi level pinning and therefore, will not affect OER.

3.3 The impact of i-SS

Experimental studies on photoanodes have reported the existence of a capacitance around OER onset.[19,22] This capacitance is proposed to be due to the presence of OER intermediates (i-SS). Klahr et al.[22,26] have reported FLP associated with the capacitance due to i-SS based on Mott-Schottky analysis. Accordingly, there is some potential drop over the charging of i-SS which lowers the potential across the space charge region.[22] In this section, we analyze, whether OER intermediates result in a capacitance as proposed in the experiments and if so, whether this capacitance can affect the potential across the space charge region. If the potential drop over i-SS is large, this will hinder the OER performance. The impact of i-SS on the PEC data is investigated by varying the rate of OER. This is done by individually varying a) the illumination intensity and b) the backward rate constants for the intermediate steps in OER.

3.3.1 Impact of the illumination intensity

The capacitance due to the accumulation of charge carriers in OER intermediates ($C_{\mathrm{i-SS}}$) is calculated according to Eq. (12). The $C_{\mathrm{i-SS}}$ for three different illumination intensities are calculated (same conditions as in Figure 3) and are plotted as a function of applied potential in Figure 5a. The $C_{\mathrm{i-SS}}$ curves have a maximum around the onset potential of the j-V curves in Figure 3. For better illustration, $C_{\mathrm{i-SS}}$ at 1 Sun illumination is plotted together with the corresponding current density in Figure 5b. The result proves that OER intermediates result in a surface state capacitance around the OER onset. The maxima of $C_{\mathrm{i-SS}}$ lie between 400 μF/cm^2 and 500 μF/cm^2 and are comparable to the literature where values between 100 μF/cm^2 and 1 mF/cm^2 have been reported.[19,22,68,69] The simulated capacitance profiles are also comparable to the literature.[19] Furthermore, with an increase in illumination intensity, the maximum capacitance increases, and the potential corresponding to the maximum capacitance decreases, which is in qualitative agreement with the literature.[22] According to Eq. (12), $C_{\mathrm{i-SS}}$ depends on the rate of formation of OER intermediates and the number of adsorption sites at the SEI. Since the number of adsorption sites remains constant for a given surface, the increase in capacitance with illumination intensity is due to the increase in the rate of formation of surface intermediates with illumination intensity. The magnitude of $C_{\mathrm{i-SS}}$ is observed to be an order of magnitude higher than that of $C_{\mathrm{r-SS}}$.

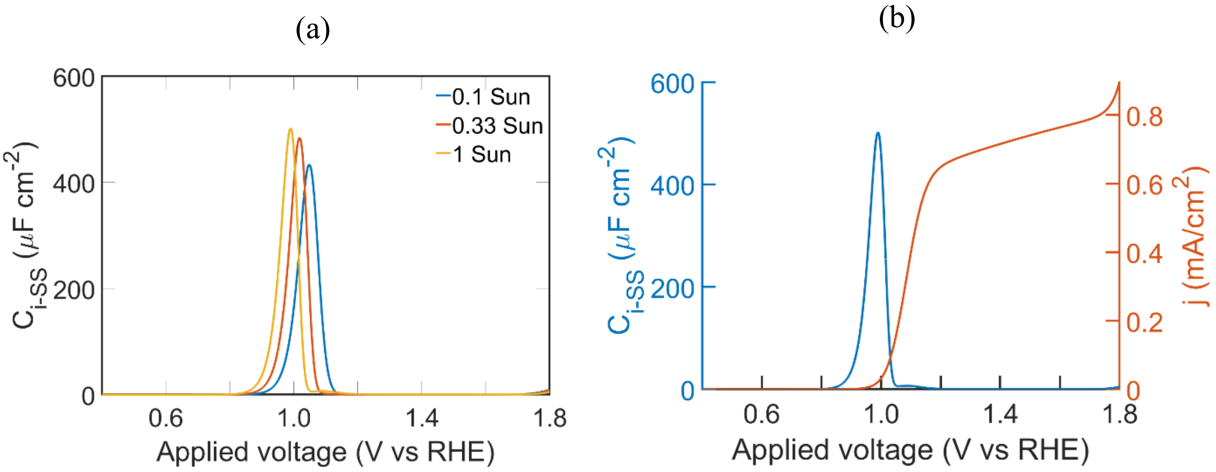

Figure 5 a) Capacitance due to i-SS simulated at different illumination intensities; b) capacitance due to i-SS and current density as a function of applied potential for 1 Sun illumination. The plot shows that the capacitance due to i-SS is observed around the OER onset potential.

The impact of $C_{\mathrm{i-SS}}$ on the potential distribution in the space charge region is investigated using Mott-Schottky analysis. The Mott-Schottky plots are generated for three different illumination intensities as shown in Figure 6a (all the model parameters are the same as in Figure 3 and Figure 5a). Two deviations from a linear behavior are found in the investigated potential range. The first deviation is a plateau around an applied potential of 0.6 V to 0.8 V vs. RHE. It is related to r-SS as discussed in the previous section.

The second deviation is comparatively smaller and starts around 1.0 V vs. RHE as shown in the enlarged plot in Figure 6b. The flattening increases as the illumination increases. The potential range of this flattening coincides with the potential range of the $C_{\mathrm{i-SS}}$ peaks in Figure 5a. A similar effect is reported in experimental studies in the literature and is interpreted as FLP due to i-SS.[70] However, we find that this flattening vanishes when the series resistance in the model is set to zero for any illumination intensity (Figure S3). This means that this second flattening cannot be interpreted as FLP due to i-SS. The reason for the flattening can be explained as follows. The current density increases directly after the onset potential as shown in Figure 3. This leads to an increase in the IR drop (V_{IR}) according to Eq. (8) and decrease in u_{sc} according to Eq. (6). According to Eq. (13), the decrease in u_{sc} leads to a decrease in $1/C_{\mathrm{sc}}^2$. This is observed as a flattening in the Mott-Schottky plot around the onset potential, as there is a sudden ramp in current density and V_{IR}, directly after the onset potential. In Figure 6b, this flattening looks like FLP, but it is in fact related to the decrease in u_{sc} due to increase in V_{IR}. This is in agreement with the experimental study by Shavorskiy et al. [31] in which a deviation in band bending was attributed to the IR drop of the measurement setup. When the illumination intensity is increased, the current density in the circuit increases as shown in Figure 3. For this reason, the IR drop and the second flattening increase with an increase in illumination intensity as shown in Figure 6b.

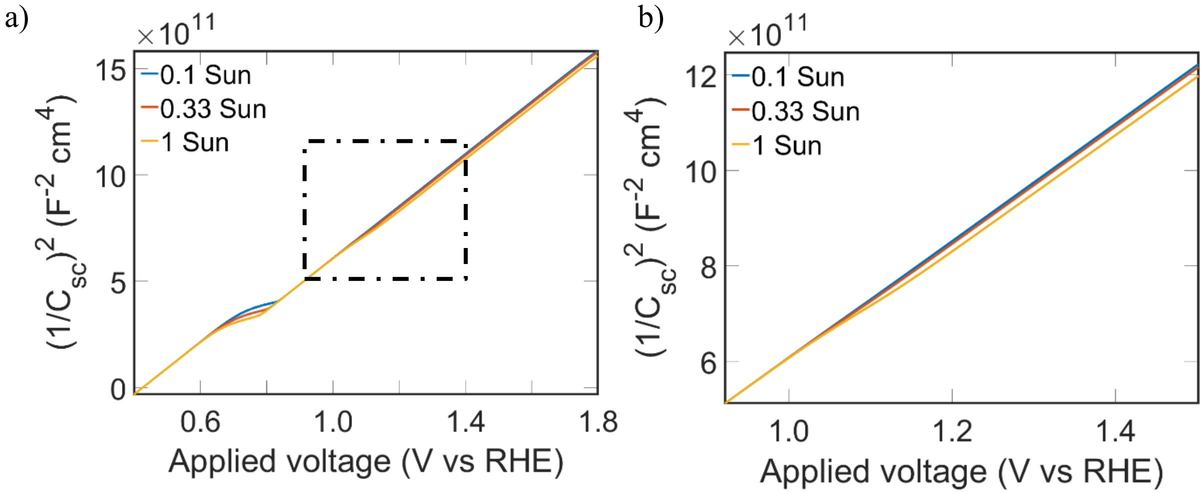

Figure 6 a) Mott-Schottky plots showing FLP due to r-SS and flattening around onset potential (shown in the box); b) Enlarged Mott-Schottky plot of a) around the onset potential to show the increase in pinning with an increase in illumination intensity; the plot area is same as the portion highlighted with the box in Figure 6a.

It is important to note that our investigations are based on the standard assumption that the Helmholtz capacitance is constant.[3,26] Based on this standard assumption, the presence of surface adsorbates (i-SS) does not affect the Helmholtz capacitance. In the literature, it has been reported that surface adsorption can, however, affect the Helmholtz capacitance.[71] This will result in C_{H} being potential dependent through the potential dependence of surface coverage. The effect of this coverage dependent C_{H} is discussed in the supporting information in section S5 "Coverage dependent Helmholtz capacitance" using a simplified model.[65] Additionally, the model considers only the intermediates involved in OER for i-SS. If species are adsorbed on the surface which are not related to OER and are not reactive, such surface states may lead to lower performance, as they block the reactive sites at the photoanode surface.

3.3.2 Impact of the backward rate constants of the intermediate steps in OER

The magnitude of $C_{\mathrm{i-SS}}$ depends on the rate of formation of OER intermediates according to Eq. (12). Therefore, $C_{\mathrm{i-SS}}$ is related to the catalysis of OER on the semiconductor surface. In this section, the rate constant for backward reactions in OER is increased and it is investigated how this impacts the current density. The backward rate constants for elementary reaction steps in OER is equivalent to the recombination rate in the case of i-SS.[32] In experiments, the recombination phenomenon is investigated using current density measured under chopped light.[23] The measurement is called a chopped light measurement (CLM). We simulate CLMs with two different backward rate constants; a potential scan rate of 20 mV/s and light on/off pulses with a pulse time of 1 s is used. Additionally, the photocurrent and dark current for the same case is calculated.

Figure 7a and Figure 7b show the CLM, the photocurrent, and the dark current simulated for $N_{\mathrm{T}} = 10^{13}\mathrm{cm}^{-2}$ with two different backward rate constants. The backward rate constants of all the four steps are changed by changing the pre-multiplier for the backward rate constants (supporting information S1.2). The pre-multipliers are chosen as $1 \cdot k_{\mathrm{v,max,b}}$ and $10^3 \cdot k_{\mathrm{v,max,b}}$. The pre-multiplier for the forward rate constants, $k_{\mathrm{v,max,f}}$, is kept the same in both cases. Thus, the ratio $k_{\mathrm{v,max,b}}/k_{\mathrm{v,max,f}}$ is three orders of magnitude higher for Figure 7b compared to Figure 7a. The surface state capacitances associated with both cases are plotted along with the corresponding photocurrent densities in Figure 7c.

The plot in Figure 7a shows no cathodic or anodic peaks near the OER onset. When $k_{\mathrm{v,max,b}}/k_{\mathrm{v,max,f}}$ is increased by three orders of magnitude, the CLM shows both anodic and cathodic peaks near the OER onset (Figure 7b). Thus, the positive (anodic) and negative (cathodic) overshoots in the CLM near the onset potential are sensitive to the rate constants of the intermediate steps in OER steps. The cathodic peak in Figure 7b increases, as a higher backward reaction increases the reduction of adsorbed intermediates, and subsequently the cathodic current.

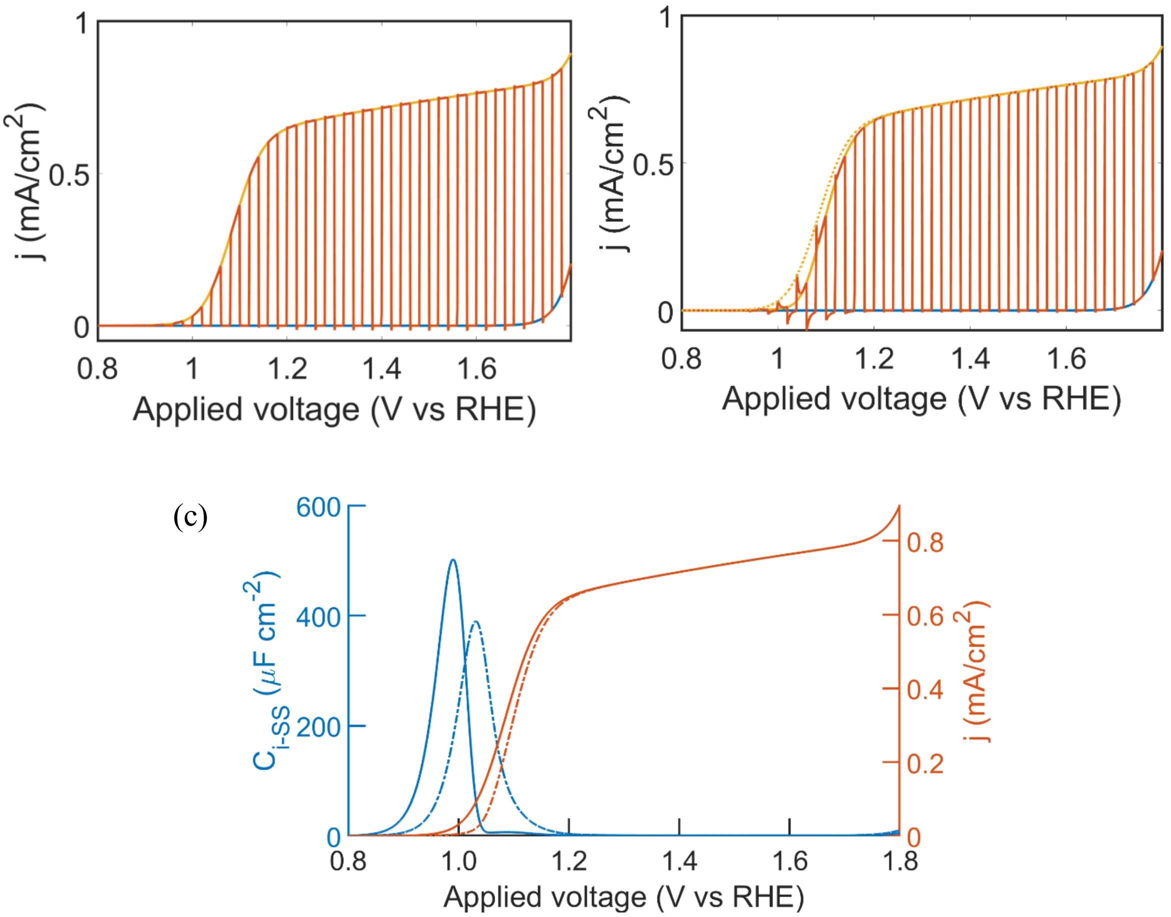
(a)

(b)

(c)

Figure 7 Simulations of chopped light measurements (red), current densities under illumination (yellow) and current densities in the dark (blue) with backward rate constant as a) $1 \cdot k_{\mathrm{v,max,b}}$ and b) $10^3 \cdot k_{\mathrm{v,max,b}}$; the current density under illumination with $1 \cdot k_{\mathrm{v,max,b}}$ is shown as a dotted line for comparison; c) the plot of the capacitances and current densities for $1 \cdot k_{\mathrm{v,max,b}}$ (bold line) and $10^3 \cdot k_{\mathrm{v,max,b}}$ (dotted line) plotted as a function of applied potential.

The reason behind the increase in anodic peak is related to the reduction in the photocurrent density with the increase in the backward reaction rate. The current density under illumination from Figure 7a is shown as a dotted line in Figure 7b for comparison; the difference in the current densities (bold yellow line and dotted yellow line) is found only near the onset potential. Under chopped light conditions, when illumination is turned on, the current density rapidly increases due to the forward reaction rate. However, due to the higher backward reaction rate, the current density settled down to the lower equilibrium value. This explains the anodic peaks in the CLM when the backward reaction rate is increased. Thus, we show that the rate of OER intermediate reactions, especially the ratio between backward and forward reaction has an impact on the anodic and cathodic current peaks in CLM found near the OER onset potential. The presence of overshoots in the current density near the onset potential is an indication of a higher ratio between backward and forward reaction which in turn indicates inferior OER catalysis; the higher the ratio is, the higher the overshoots are. Such an insight about the impact of the rate constants of the intermediate steps on PEC data is challenging to obtain from experiments. This is due to the challenges associated with the experimental identification of OER intermediates. However, with our approach, we can simulate the impact of OER intermediate reactions on PEC data.

Figure 7c shows a combined plot of the surface state capacitance and the current densities for the two rate constants. The maximum of $C_{\mathrm{i-SS}}$ decreases and the peak position shifts to a higher potential with an increase in the backward rate constant. The comparison of the photocurrent densities shows that the onset potential increases with an increase in the backward rate constant. A higher backward reaction rate is unfavorable for OER and leads to a lower catalytic performance of OER on the photoanode surface. Only the onset potential is affected in this regard and the saturation current density is unaffected. According to the literature, the onset potential is determined by the catalysis of the surface,[72] Therefore according to Figure

7c, a decrease in $C_{\mathrm{i-SS}}$ found for example in experimental data can be an indication of a decrease in the catalytic performance of the photoanode surface. At higher potentials the forward reaction dominates as the hole density increases with the applied potential. As $C_{\mathrm{i-SS}}$ does not affect u_{sc}, the hole density at higher potentials is not affected which explains the constant saturation current density in both cases.

4 Summary

A microkinetic model based on a multistep OER mechanism which also takes into account the charge carrier dynamics within the semiconductor is developed. This model allows simulating and understanding the impact of the recombining surface states (r-SS) and intermediate surface states (i-SS) on typical PEC measurement data. The impact of r-SS and i-SS on the PEC data, such as j-V plots, surface state capacitance, Mott-Schottky plots, hole flux, and chopped light current, are investigated with the model. The features in the PEC data arising due to r-SS and i-SS are discussed by analyzing the sensitivity of the data to the parameters related to r-SS and i-SS. The results regarding r-SS and i-SS are summarized in Figure 8; findings related to r-SS are shown in red color, while findings related to i-SS are shown in blue color.

We found that both r-SS and i-SS result in capacitive behavior with their maximum capacitances at characteristic applied voltages (Figure 8a): $C_{\mathrm{r-SS}}$ culminates typically below the onset potential, while $C_{\mathrm{i-SS}}$ culminates around the onset potential. Hence, we claim that the location of the capacitance peaks along the potential axis is a measure to distinguish r-SS and i-SS. Additionally, the magnitude of the peak of $C_{\mathrm{r-SS}}$ is an order of magnitude lower than that of $C_{\mathrm{i-SS}}$. Both these findings are important and help to distinguish between r-SS and i-SS in experimental studies. As the surface state density (N_{T}) increases, the maximum of $C_{\mathrm{r-SS}}$ increases and the $C_{\mathrm{r-SS}}$ peak shifts to a higher potential. The maximum of $C_{\mathrm{i-SS}}$ depends on the illumination intensity (I_0) and on the rate constants of the intermediate steps in OER (k_{OER}). The results are in agreement with experiments.[7,21,22]

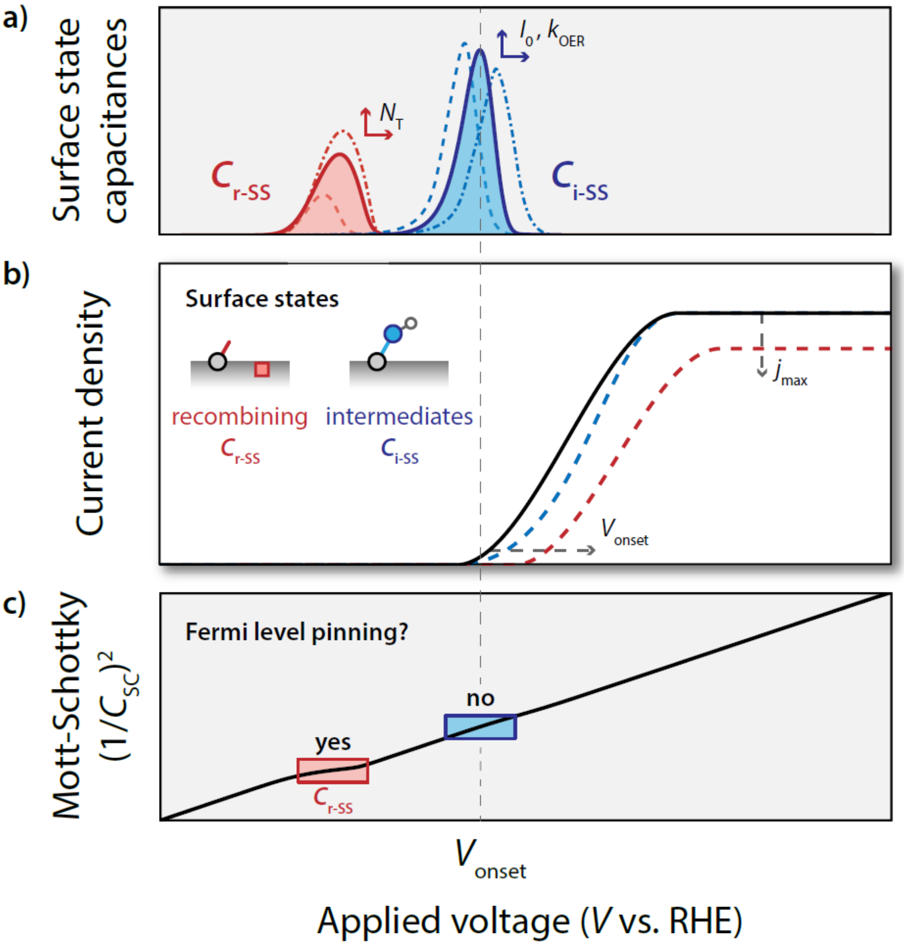

Figure 8 a) A representative plot showing the relative magnitudes and positions of surface state capacitances (C_{r-SS} and C_{i-SS}) along the potential axis. For an increase in N_T, the maximum of $C_{\mathrm{r-SS}}$ increases and shifts to higher potential as N_T is increased. The maximum of $C_{\mathrm{i-SS}}$ depends on the illumination intensity (I_0) and the rate constants of the intermediate steps in OER; b) j-V characteristic showing an increase in onset potential and a decrease in saturation current density with an increase in C_{r-SS}; the onset potential increases with a decrease in C_{i-SS}; c) Mott-Schottky plot shows Fermi level pinning corresponding to r-SS and no Fermi level pinning corresponding to i-SS; the flattening in the Mott-Schottky plot observed around the onset potential is related to potential drop over R_s.

The impact of r-SS and i-SS on the current density is shown in Figure 8b. The presence of r-SS leads to a delayed onset potential and lower saturation current density. In the case of i-SS, a lower magnitude of $C_{\mathrm{i-SS}}$ leads to a slightly delayed onset of current density; the saturation current density is not affected by i-SS. Our study shows that the correlation between the surface state capacitances and OER performance is different for r-SS and i-SS; an increase in the magnitude of $C_{\mathrm{r-SS}}$ peak leads to lower photoanode performance, whereas, in the case of $C_{\mathrm{i-SS}}$, the increase in the magnitude indicates improved OER catalysis which leads to lower onset potential.

In Mott-Schottky analysis (Figure 8c), we found deviations from the linear behavior at the same potentials as that of the maxima of the surface state capacitances. The deviation at low potential (shown in red) is related to r-SS and is attributed to Fermi level pinning (FLP) which is in agreement with experimental studies.[7] Hence, r-SS reduces the potential available across the space charge region which explains the higher onset potential and lower saturation current density as found in Figure 8b. The deviation from the linear behavior in the Mott-Schottky plot around the onset potential (shown in blue) is less visible and it is located in the same potential range as $C_{\mathrm{i-SS}}$. However, this deviation is not related to i-SS but due to the potential drop over R_{s} in the circuit. This deviation in the Mott-Schottky plot can get interpreted in the analysis of PEC data as FLP due to i-SS, since the potential range of the deviation coincides with that of $C_{\mathrm{i-SS}}$. We will discuss the impact of R_s on PEC measurements in more detail in a forthcoming publication.

The results show that the analysis of PEC experimental data in combination with a microkinetic model of OER gives additional insights into the catalysis of OER at the photoanode surface. Based on our analysis, we found that r-SS reduces photoanode performance (Figure 8). Therefore, it is necessary to remove such surface states to lower the onset potential and thus to enhance the photoanode performance. Selective removal of surface states using high-temperature annealing has been reported in the literature in the case of hematite photoanodes.[7]

The results in this study are based on the simulations for hematite photoanode material. However, the model is generic and can be applied to OER on other photoanode materials, like TiO_2 or Ta_3N_5. This can be done by substituting the corresponding material-specific optoelectronic parameters like bandgap, band edge positions, and absorption coefficient in the model. The theoretical rate constants for the intermediate steps at the surface of the chosen material are also required for the simulation. These can be calculated based on the free energies of formation of OER intermediates at the surface obtained from DFT calculations. The model can be used to compare different photoanode materials, based on their optoelectronic properties. Comparison based on simulations is easier compared to experiments as simulations are faster and cost-effective compared to performing experiments on several materials. In this way, the model can contribute in the future to identify photoanode materials with the potential for high performance.

The model discussed here combines for the first time multistep OER at the semiconductor surface and charge carrier dynamics within the semiconductor. This is an important step to realistically simulate the processes at the photoelectrode – electrolyte interface. Further development of the model in combination with experiments will improve the understanding of the processes that take place at the semiconductor-electrolyte interface during OER, which are challenging to deconvolute experimentally.

ASSOCIATED CONTENT

Supporting Information.

The following files are available free of charge.

Detailed microkinetic model based on the multistep mechanism of OER, constants used and supplementary figures (PDF).

Relaxed geometries of hematite surface with OER intermediates (ZIP)

AUTHOR INFORMATION

Corresponding Author

* Email: a.bieberle@differ.nl

[4] Eindhoven University of Technology, Mechanical Engineering, Control Systems Technology, PO Box 513, 5600 MB Eindhoven, The Netherlands.

[5] Delft University of Technology, Process and Energy Department, Faculty of Mechanical, Maritime and Materials Engineering, Leeghwaterstraat 39, 2628CB, Delft, The Netherlands.

Author Contributions

The manuscript was written through the contributions of all authors. All authors have approved the final version of the manuscript.

Notes

The authors declare no competing financial interest.

Acknowledgments

George acknowledges funding from the Shell-NWO/FOM "Computational Sciences for Energy Research" PhD program (CSER-PhD; nr. i32; project number 15CSER021). Bieberle-Hütter and Sinha acknowledge the financial support from NWO (FOM program nr. 147 "CO_2 neutral fuels") and M-ERA. NET (project "MuMo4PEC" no. 4089). Supercomputing facilities of the Dutch national supercomputers SURFsara/Lisa and Cartesius are acknowledged. Erik Langereis is acknowledged for graphical support. Prof. Michiel Sprik (University of

Cambridge, UK), Prof. dr. Evert Jan Meijer (University of Amsterdam, Netherlands), and Dr. Rochan Sinha are acknowledged for the fruitful discussions regarding model development.

References

(1) Wickman, B.; Bastos Fanta, A.; Burrows, A.; Hellman, A.; Wagner, J. B.; Iandolo, B. Iron Oxide Films Prepared by Rapid Thermal Processing for Solar Energy Conversion. *Sci. Rep.* **2017**, *7*, 1–9.

(2) Chu, S.; Li, W.; Yan, Y.; Hamann, T.; Shih, I.; Wang, D.; Mi, Z. Roadmap on Solar Water Splitting: Current Status and Future Prospects. *Nano Futur.* **2017**, *1*.

(3) van de Krol, R. Principles of Photoelectrochemical Cells. In *Photoelectrochemical Hydrogen Production*; van de Krol, R., Grätzel, M., Eds.; Springer US: Boston, MA, 2012; pp 13–67.

(4) Bachmann, J.; Haschke, S.; Barth, J. A. C.; Mader, M.; Angeles-Boza, A. M.; Roberts, A. M.; Schlicht, S. Direct Oxygen Isotope Effect Identifies the Rate-Determining Step of Electrocatalytic OER at an Oxidic Surface. *Nat. Commun.* **2018**, *9*.

(5) Zhang, X.; Bieberle-Hütter, A. Modeling and Simulations in Photoelectrochemical Water Oxidation: From Single Level to Multiscale Modeling. *ChemSusChem* **2016**, *9*, 1223–1242.

(6) Friebel, D.; Louie, M. W.; Bajdich, M.; Sanwald, K. E.; Cai, Y.; Wise, A. M.; Cheng, M. J.; Sokaras, D.; Weng, T. C.; Alonso-Mori, R.; Davis, R. C.; Bargar, J. R.; Nørskov, J. K.; Nilsson, A.; Bell, A. T. Identification of Highly Active Fe Sites in (Ni,Fe)OOH for Electrocatalytic Water Splitting. *J. Am. Chem. Soc.* **2015**, *137*, 1305–1313.

(7) Zandi, O.; Hamann, T. W. Enhanced Water Splitting Efficiency through Selective Surface State Removal. *J. Phys. Chem. Lett.* **2014**, *5*, 1522–1526.

(8) Yang, X.; Liu, R.; Lei, Y.; Li, P.; Wang, K.; Zheng, Z.; Wang, D. Dual Influence of Reduction Annealing on Diffused Hematite/FTO Junction for Enhanced

Photoelectrochemical Water Oxidation. *ACS Appl. Mater. Interfaces* **2016**, *8*, 16476–16485.

(9) van de Krol, R.; Liang, Y.; Schoonman, J. Solar Hydrogen Production with Nanostructured Metal Oxides. *J. Mater. Chem.* **2008**, *18*, 2311.

(10) Formal, F. Le; Grätzel, M.; Sivula, K. Controlling Photoactivity in Ultrathin Hematite Films for Solar Water-Splitting. *Adv. Funct. Mater.* **2010**, *20*, 1099–1107.

(11) Dotan, H.; Sivula, K.; Grätzel, M.; Rothschild, A.; Warren, S. C. Probing the Photoelectrochemical Properties of Hematite (α-Fe 2O3) Electrodes Using Hydrogen Peroxide as a Hole Scavenger. *Energy Environ. Sci.* **2011**, *4*, 958–964.

(12) Dias, P.; Lopes, T.; Meda, L.; Andrade, L.; Mendes, A. Photoelectrochemical Water Splitting Using WO3 Photoanodes: The Substrate and Temperature Roles. *Phys. Chem. Chem. Phys.* **2016**, *18*, 5232–5243.

(13) Wang, G.; Ling, Y.; Wang, H.; Yang, X.; Wang, C.; Zhang, J. Z.; Li, Y. Hydrogen-Treated WO3 Nanoflakes Show Enhanced Photostability. *Energy Environ. Sci.* **2012**, *5*, 6180.

(14) Ding, C.; Shi, J.; Wang, D.; Wang, Z.; Wang, N.; Liu, G.; Xiong, F.; Li, C. Visible Light Driven Overall Water Splitting Using Cocatalyst/BiVO4 Photoanode with Minimized Bias. *Phys. Chem. Chem. Phys.* **2013**, *15*, 4589.

(15) Liang, Y.; Tsubota, T.; Mooij, L. P. A.; Van De Krol, R. Highly Improved Quantum Efficiencies for Thin Film BiVO4 Photoanodes. *J. Phys. Chem. C* **2011**, *115*, 17594–17598.

(16) Dotan, H.; Kfir, O.; Sharlin, E.; Blank, O.; Gross, M.; Dumchin, I.; Ankonina, G.;

Rothschild, A. Resonant Light Trapping in Ultrathin Films for Water Splitting. *Nat. Mater.* **2013**, *12*, 158–164.

(17) Tamirat, A. G.; Rick, J.; Dubale, A. A.; Su, W. N.; Hwang, B. J. Using Hematite for Photoelectrochemical Water Splitting: A Review of Current Progress and Challenges. *Nanoscale Horizons* **2016**, *1*, 243–267.

(18) Thorne, J. E.; Jang, J. W.; Liu, E. Y.; Wang, D. Understanding the Origin of Photoelectrode Performance Enhancement by Probing Surface Kinetics. *Chem. Sci.* **2016**, *7*, 3347–3354.

(19) Wang, Z.; Fan, F.; Wang, S.; Ding, C.; Zhao, Y.; Li, C. Bridging Surface States and Current-Potential Response over Hematite-Based Photoelectrochemical Water Oxidation. *RSC Adv.* **2016**, *6*, 85582–85586.

(20) Klahr, B.; Hamann, T. Water Oxidation on Hematite Photoelectrodes: Insight into the Nature of Surface States through in Situ Spectroelectrochemistry. *J. Phys. Chem. C* **2014**, *118*, 10393–10399.

(21) Palmolahti, L.; Ali-Löytty, H.; Khan, R.; Saari, J.; Tkachenko, N. V.; Valden, M. Modification of Surface States of Hematite-Based Photoanodes by Submonolayer of TiO 2 for Enhanced Solar Water Splitting . *J. Phys. Chem. C* **2020**, *124*, 13094–13101.

(22) Klahr, B.; Gimenez, S.; Fabregat-Santiago, F.; Bisquert, J.; Hamann, T. W. Electrochemical and Photoelectrochemical Investigation of Water Oxidation with Hematite Electrodes. *Energy Environ. Sci.* **2012**, *5*, 7626–7636.

(23) Peter, L. M. Energetics and Kinetics of Light-Driven Oxygen Evolution at Semiconductor Electrodes: The Example of Hematite. *J. Solid State Electrochem.* **2013**, *17*, 315–326.

(24) Upul Wijayantha, K. G.; Saremi-Yarahmadi, S.; Peter, L. M. Kinetics of Oxygen Evolution at α-Fe2O3 Photoanodes: A Study by Photoelectrochemical Impedance Spectroscopy. *Phys. Chem. Chem. Phys.* **2011**, *13*, 5264.

(25) Zandi, O.; Hamann, T. W. The Potential versus Current State of Water Splitting with Hematite. *Phys. Chem. Chem. Phys.* **2015**, *17*, 22485–22503.

(26) Klahr, B.; Gimenez, S.; Fabregat-Santiago, F.; Hamann, T.; Bisquert, J. Water Oxidation at Hematite Photoelectrodes: The Role of Surface States. *J. Am. Chem. Soc.* **2012**, *134*, 4294–4302.

(27) Le Formal, F.; Sivula, K.; Grätzel, M. The Transient Photocurrent and Photovoltage Behavior of a Hematite Photoanode under Working Conditions and the Influence of Surface Treatments. *J. Phys. Chem. C* **2012**, *116*, 26707–26720.

(28) Du, C.; Zhang, M.; Jang, J. W.; Liu, Y.; Liu, G. Y.; Wang, D. Observation and Alteration of Surface States of Hematite Photoelectrodes. *J. Phys. Chem. C* **2014**, *118*, 17054–17059.

(29) Tamirat, A. G.; Rick, J.; Dubale, A. A.; Su, W. N.; Hwang, B. J. Using Hematite for Photoelectrochemical Water Splitting: A Review of Current Progress and Challenges. *Nanoscale Horizons* **2016**, *1*, 243–267.

(30) Zhang, Y.; Zhang, H.; Liu, A.; Chen, C.; Song, W.; Zhao, J. Rate-Limiting O-O Bond Formation Pathways for Water Oxidation on Hematite Photoanode. *J. Am. Chem. Soc.* **2018**, *140*, 3264–3269.

(31) Shavorskiy, A.; Ye, X.; Karslloğlu, O.; Poletayev, A. D.; Hartl, M.; Zegkinoglou, I.; Trotochaud, L.; Nemšák, S.; Schneider, C. M.; Crumlin, E. J.; Axnanda, S.; Liu, Z.; Ross, P. N.; Chueh, W.; Bluhm, H. Direct Mapping of Band Positions in Doped and

Undoped Hematite during Photoelectrochemical Water Splitting. *J. Phys. Chem. Lett.* **2017**, *8*, 5579–5586.

(32) Zandi, O.; Hamann, T. W. Determination of Photoelectrochemical Water Oxidation Intermediates on Haematite Electrode Surfaces Using Operando Infrared Spectroscopy. *Nat. Chem.* **2016**, *8*, 778–783.

(33) George, K.; van Berkel, M.; Zhang, X.; Sinha, R.; Bieberle-Hütter, A. Impedance Spectra and Surface Coverages Simulated Directly from the Electrochemical Reaction Mechanism: A Nonlinear State-Space Approach. *J. Phys. Chem. C* **2019**, *123*, 9981–9992.

(34) Bertoluzzi, L.; Badia-Bou, L.; Fabregat-Santiago, F.; Gimenez, S.; Bisquert, J. Interpretation of Cyclic Voltammetry Measurements of Thin Semiconductor Films for Solar Fuel Applications. *J. Phys. Chem. Lett.* **2013**, *4*, 1334–1339.

(35) Kelly, J. J.; Memming, R. The Influence of Surface Recombination and Trapping on the Cathodic Photocurrent at P-Type III-V Electrodes. *J. Electrochem. Soc.* **1982**, *129*, 730–738.

(36) Singh, M. R.; Haussener, S.; Weber, A. Z. Continuum-Scale Modeling of Solar Water-Splitting Devices. In *Integrated Solar Fuel Generators*; Royal Society of Chemistry, 2018; pp 500–536.

(37) Koper, M. T. M. Thermodynamic Theory of Multi-Electron Transfer Reactions: Implications for Electrocatalysis. *J. Electroanal. Chem.* **2011**, *660*, 254–260.

(38) Rossmeisl, J.; Qu, Z. W.; Zhu, H.; Kroes, G. J.; Nørskov, J. K. Electrolysis of Water on Oxide Surfaces. *J. Electroanal. Chem.* **2007**, *607*, 83–89.

(39) Hellman, A.; Iandolo, B.; Wickman, B.; Grönbeck, H.; Baltrusaitis, J. Electro-Oxidation of Water on Hematite: Effects of Surface Termination and Oxygen Vacancies Investigated by First-Principles. *Surf. Sci.* **2015**, *640*, 45–49.

(40) Gono, P.; Pasquarello, A. Oxygen Evolution Reaction: Bifunctional Mechanism Breaking the Linear Scaling Relationship. *J. Chem. Phys.* **2020**, *152*, 104712.

(41) Rüdiger, M. Electron Transfer Theories. In *Semiconductor Electrochemistry*; Wiley-Blackwell, 2015; pp 127–168.

(42) Barroso, M.; Pendlebury, S. R.; Cowan, A. J.; Durrant, J. R. Charge Carrier Trapping, Recombination and Transfer in Hematite (α-Fe2O3) Water Splitting Photoanodes. *Chem. Sci.* **2013**, *4*, 2724.

(43) Hellman, A.; Iandolo, B.; Wickman, B.; Grönbeck, H.; Baltrusaitis, J. Electro-Oxidation of Water on Hematite: Effects of Surface Termination and Oxygen Vacancies Investigated by First-Principles. *Surf. Sci.* **2015**, *640*, 45–49.

(44) Gerischer, H. Charge Transfer Processes at Semiconductor-Electrolyte Interfaces in Connection with Problems of Catalysis. *Surf. Sci.* **1969**, *18*, 97–122.

(45) Klahr, B. M.; Hamann, T. W. Current and Voltage Limiting Processes in Thin Film Hematite Electrodes. *J. Phys. Chem. C* **2011**, *115*, 8393–8399.

(46) Gärtner, W. W. Depletion-Layer Photoeffects in Semiconductors. *Phys. Rev.* **1959**, *116*, 84–87.

(47) Rüdiger, M. Charge Transfer Processes at the Semiconductor–Liquid Interface. In *Semiconductor Electrochemistry*; Wiley-Blackwell, 2015; pp 169–266.

(48) Cendula, P.; David Tilley, S.; Gimenez, S.; Bisquert, J.; Schmid, M.; Grätzel, M.;

Schumacher, J. O. Calculation of the Energy Band Diagram of a Photoelectrochemical Water Splitting Cell. *J. Phys. Chem. C* **2014**, *118*, 29599–29607.

(49) García-Osorio, D. A.; Jaimes, R.; Vazquez-Arenas, J.; Lara, R. H.; Alvarez-Ramirez, J. The Kinetic Parameters of the Oxygen Evolution Reaction (OER) Calculated on Inactive Anodes via EIS Transfer Functions: • OH Formation. *J. Electrochem. Soc.* **2017**, *164*, E3321–E3328.

(50) Klahr, B. M.; Hamann, T. W. Voltage Dependent Photocurrent of Thin Film Hematite Electrodes. *Appl. Phys. Lett.* **2011**, *99*, 2011–2014.

(51) Hankin, A.; Bedoya-Lora, F. E.; Alexander, J. C.; Regoutz, A.; Kelsall, G. H. Flat Band Potential Determination: Avoiding the Pitfalls. *J. Mater. Chem. A* **2019**, *7*, 26162–26176.

(52) Klotz, D.; Ellis, D. S.; Dotan, H.; Rothschild, A. Empirical: In Operando Analysis of the Charge Carrier Dynamics in Hematite Photoanodes by PEIS, IMPS and IMVS. *Phys. Chem. Chem. Phys.* **2016**, *18*, 23438–23457.

(53) Singh, P.; Rajeshwar, K.; DuBow, J.; Singh, R. Estimation of Series Resistance Losses and Ideal Fill Factors for Photoelectrochemical Cells. *J. Electrochem. Soc.* **1981**, *128*, 1396–1398.

(54) Iandolo, B.; Hellman, A. The Role of Surface States in the Oxygen Evolution Reaction on Hematite. *Angew. Chemie - Int. Ed.* **2014**, *53*, 13404–13408.

(55) Segev, G.; Dotan, H.; Malviya, K. D.; Kay, A.; Mayer, M. T.; Grätzel, M.; Rothschild, A. High Solar Flux Concentration Water Splitting with Hematite (α-Fe2O3) Photoanodes. *Adv. Energy Mater.* **2016**, *6*, 1–7.

(56) Shinde, P. S.; Annamalai, A.; Kim, J. H.; Choi, S. H.; Lee, J. S.; Jang, J. S. Exploiting the Dynamic Sn Diffusion from Deformation of FTO to Boost the Photocurrent Performance of Hematite Photoanodes. *Sol. Energy Mater. Sol. Cells* **2015**, *141*, 71–79.

(57) Annamalai, A.; Subramanian, A.; Kang, U.; Park, H.; Choi, S. H.; Jang, J. S. Activation of Hematite Photoanodes for Solar Water Splitting: Effect of FTO Deformation. *J. Phys. Chem. C* **2015**, *119*, 3810–3817.

(58) Klotz, D.; Grave, D. A.; Rothschild, A. Accurate Determination of the Charge Transfer Efficiency of Photoanodes for Solar Water Splitting. *Phys. Chem. Chem. Phys.* **2017**, *19*, 20383–20392.

(59) Bisquert, J. Theory of the Impedance of Charge Transfer via Surface States in Dye-Sensitized Solar Cells. *J. Electroanal. Chem.* **2010**, *646*, 43–51.

(60) Shampine, L. F.; Reichelt, M. W. Ode_Suite. *J. Sci. Comput.* **1997**, *18*, 1–22.

(61) Zhang, X.; Cao, C.; Bieberle-Hütter, A. Orientation Sensitivity of Oxygen Evolution Reaction on Hematite. *J. Phys. Chem. C* **2016**, *120*, 28694–28700.

(62) van de Krol, R. Photoelectrochemical Measurements. In *Photoelectrochemical Hydrogen Production*; van de Krol, R., Grätzel, M., Eds.; Springer US: Boston, MA, 2012; pp 69–117.

(63) Shavorskiy, A.; Ye, X.; Karslloğlu, O.; Poletayev, A. D.; Hartl, M.; Zegkinoglou, I.; Trotochaud, L.; Nemšák, S.; Schneider, C. M.; Crumlin, E. J.; Axnanda, S.; Liu, Z.; Ross, P. N.; Chueh, W.; Bluhm, H. Direct Mapping of Band Positions in Doped and Undoped Hematite during Photoelectrochemical Water Splitting. *J. Phys. Chem. Lett.* **2017**, *8*, 5579–5586.

(64) Peter, L. M. Dynamic Aspects of Semiconductor Photoelectrochemistry. *Chem. Rev.* **1990**, *90*, 753–769.

(65) Bard, A. J.; Bocarsly, A. B.; Fan, F. R. F.; Walton, E. G.; Wrighton, M. S. The Concept of Fermi Level Pinning at Semiconductor/Liquid Junctions. Consequences for Energy Conversion Efficiency and Selection of Useful Solution Redox Couples in Solar Devices. *J. Am. Chem. Soc.* **1980**, *102*, 3671–3677.

(66) Hisatomi, T.; Le Formal, F.; Cornuz, M.; Brillet, J.; Tétreault, N.; Sivula, K.; Grätzel, M. Cathodic Shift in Onset Potential of Solar Oxygen Evolution on Hematite by 13-Group Oxide Overlayers. *Energy Environ. Sci.* **2011**, *4*, 2512–2515.

(67) Forstmann, F. The Concepts of Surface States. *Prog. Surf. Sci.* **1993**, *42*, 21–31.

(68) Ruoko, T. P.; Hiltunen, A.; Iivonen, T.; Ulkuniemi, R.; Lahtonen, K.; Ali-Löytty, H.; Mizohata, K.; Valden, M.; Leskelä, M.; Tkachenko, N. V. Charge Carrier Dynamics in Tantalum Oxide Overlayered and Tantalum Doped Hematite Photoanodes. *J. Mater. Chem. A* **2019**, *7*, 3206–3215.

(69) Le Formal, F.; Pendlebury, S. R.; Cornuz, M.; Tilley, S. D.; Grätzel, M.; Durrant, J. R. Back Electron-Hole Recombination in Hematite Photoanodes for Water Splitting. *J. Am. Chem. Soc.* **2014**, *136*, 2564–2574.

(70) Memming, R. Solid–Liquid Interface. In *Semiconductor Electrochemistry*; John Wiley & Sons, Ltd, 2015; pp 89–125.

(71) Bohra, D.; Chaudhry, J. H.; Burdyny, T.; Pidko, E. A.; Smith, W. A. Modeling the Electrical Double Layer to Understand the Reaction Environment in a CO2 Electrocatalytic System. *Energy Environ. Sci.* **2019**, *12*, 3380–3389.

(72) Sivula, K.; Le Formal, F.; Grätzel, M. Solar Water Splitting: Progress Using Hematite (α-Fe 2O3) Photoelectrodes. *ChemSusChem* **2011**, *4*, 432–449.

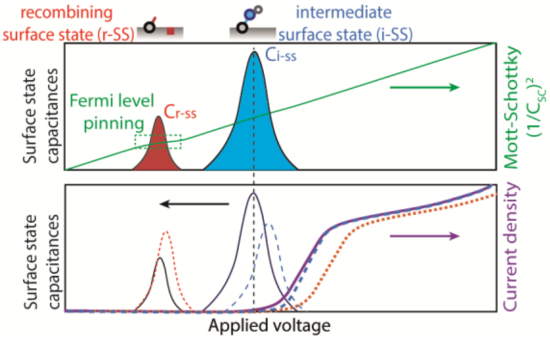
recombining surface state (r-SS)
intermediate surface state (i-SS)
$C_{i\text{-}ss}$
Surface state capacitances
Fermi level pinning
$C_{r\text{-}ss}$
Mott-Schottky $(1/C_{SC})^2$
Surface state capacitances
Current density
Applied voltage

Supporting Information:

Understanding the Impact of Different Types of Surface States on Photoelectrochemical Water Oxidation: A Microkinetic Modeling Approach

Kiran George,[1] *Tigran Khachatrjan,*[2] *Matthijs van Berkel,*[3,4] *Vivek Sinha,*[1,5] *and Anja Bieberle-Hütter*[1,]*

[1] Dutch Institute for Fundamental Energy Research (DIFFER), Electrochemical Materials and Interfaces, PO Box 6336, 5600 HH Eindhoven, The Netherlands.

[2] Eindhoven University of Technology, Department of Applied Physics, PO Box 513, 5600 MB Eindhoven, The Netherlands

[3] Dutch Institute for Fundamental Energy Research (DIFFER), Energy Systems & Control, PO Box 6336, 5600 HH Eindhoven, The Netherlands

*Corresponding author email: a.bieberle@differ.nl

S1. Microkinetic model of OER

The oxygen evolution reaction under alkaline environment is given by

$$4OH^- + 4h^+ \rightarrow O_2 + 2H_2O \tag{S.1}$$

In this study, reactions in an alkaline environment are considered and the mechanism proposed by Hellman et al.[1] is chosen. This mechanism is based on the multistep OER mechanism proposed earlier by Rossmeisl et al.[2]

S1.1 Electrochemical mechanism of OER

The four-step OER in alkaline environment is given as

$$* + OH^- + h^+ \underset{K_{\mathrm{b1}}}{\overset{K_{\mathrm{f1}}}{\rightleftharpoons}} OH_{\mathrm{ad}} \tag{S.2}$$

$$OH_{\mathrm{ad}} + OH^- + h^+ \underset{K_{\mathrm{b2}}}{\overset{K_{\mathrm{f2}}}{\rightleftharpoons}} O_{\mathrm{ad}} + H_2O \tag{S.3}$$

$$O_{\mathrm{ad}} + OH^- + h^+ \underset{K_{\mathrm{b3}}}{\overset{K_{\mathrm{f3}}}{\rightleftharpoons}} OOH_{\mathrm{ad}} \tag{S.4}$$

$$OOH_{\mathrm{ad}} + OH^- + h^+ \underset{K_{\mathrm{b4}}}{\overset{K_{\mathrm{f4}}}{\rightleftharpoons}} O_{2,\mathrm{ad}} + H_2O \tag{S.5}$$

Here * represents an adsorption site and the subscript *ad* means that the species are adsorbed on the surface. Thus, OH_{ad}, O_{ad}, OOH_{ad}, and $O_{2,\mathrm{ad}}$ are the intermediate species adsorbed on the surface during the OER. The forward and backward reaction rates of these charge transfer reactions are represented by K_{fi} and K_{bi}, respectively, where i = 1 to 4. The calculation of these rate constants is described in the following sections. After adsorbed oxygen ($O_{2,\mathrm{ad}}$) is formed at the site, it desorbs ($O_{2,\mathrm{des}}$) from the surface at a rate of K_{f5} which is given by

$$O_{2,\mathrm{ad}} \overset{K_{\mathrm{f5}}}{\rightarrow} O_{2,\mathrm{des}} + * \tag{S.6}$$

This step does not involve charge transfer and, hence, the desorption rate K_{f5} is chosen as a constant.

S1.2 Charge transfer via valence band and conduction band

Rate constants for charge transfer via valence band and conduction band

For an ideal semiconductor, charge transfer can occur via the valence band (VB) and/or via the conduction band (CB). The forward and backward rate constants for charge transfer via VB, $K_{\mathrm{v}_{\mathrm{fi}}}$ and $K_{\mathrm{v}_{\mathrm{bi}}}$ can be calculated as[3]

$$K_{\mathrm{v}_{\mathrm{fi}}} = \overline{kv_{\mathrm{f\imath}}}p_{\mathrm{s}} \tag{S.7}$$

$$K_{\mathrm{v}_{\mathrm{bi}}} = \overline{kv_{\mathrm{b\imath}}}N_{\mathrm{v}} \tag{S.8}$$

$$\overline{kv_{f\imath}} = k_{\mathrm{v,max,f}} \exp\left[-\frac{\left(E_{\mathrm{v}} - E^{0}_{\mathrm{F,redox,i}} - V_{\mathrm{H}} - \lambda\right)^{2}}{4\lambda K_{\mathrm{B}}T}\right] \tag{S.9}$$

$$\overline{kv_{b\imath}} = k_{\mathrm{v,max,b}} \exp\left[-\frac{\left(E_{\mathrm{v}} - E^{0}_{\mathrm{F,redox,i}} - V_{\mathrm{H}} + \lambda\right)^{2}}{4\lambda K_{B}T}\right] \tag{S.10}$$

where p_{s} is the hole density at the surface, N_{v} is the density of states of the valence band, E_{v} is the valence band energy level, $E_{\mathrm{redox,i}}$ is the redox potential of the intermediate steps (i = 1 to 4), V_{H} is the potential drop across the Helmholtz layer, λ is the solvent reorganization energy, k_{B} is the Boltzmann constant, and T is the temperature. The descriptions of all the parameters used in the model and their respective values are given in Table S1.

Table S1 Model parameters specific to the microkinetic model, their descriptions, and values in addition to Table 1 in the main manuscript.

Parameter	Description	Value	Ref.
K_{B}	Boltzmann constant	8.61733 x 10^{-5} eV/K	
e	Charge of electron	1.60217662 x 10^{-19} C	
ϵ_0	Permittivity of free space	8.8541878128 x 10^{-14} F cm^{-1}	
Sr	Scan rate	20 mV/s	
T	Temperature	298 K	

pH	pH of the electrolyte	13.6	
pOH	pOH of the electrolyte	14-pH	
x_{OH}	Mole fraction of hydroxyl ions	$10^{-\mathrm{pOH}}$/(molar conc. of water)	
x_{H2O}	Mole fraction of water	1-x_{OH}	
$k_{\mathrm{v,max,f}}$, $k_{\mathrm{v,max,b}}$	Max. rate constants via val. band	3×10^{-16} cm^{4}/s	4
$k_{\mathrm{c,max,f}}$, $k_{\mathrm{c,max,b}}$	Max. rate constants via cond. band	3×10^{-16} cm^{4}/s	4
$k_{\mathrm{t,max,f}}$, $k_{\mathrm{t,max,b}}$	Max. rate constants via trap state	3×10^{-16} cm^{4}/s	4
λ	Solvent reorganization energy	1 eV	5
N_{C}	Density of state of cond. band	4×10^{22} cm^{-3}	6
N_{V}	Density of state of val. band	1×10^{22} cm^{-3}	6
K_{f5}	Desorption rate of oxygen	8×10^{5} cm^{-1}	7

Similarly, the rate constants for charge transfer via CB (subscript c) can be calculated as [3]

$$K_{\mathrm{c}_{\mathrm{fi}}} = \overline{kc_{\mathrm{fi}}} N_{\mathrm{c}} \tag{S.11}$$

$$K_{c_{\mathrm{bi}}} = \overline{kc_{\mathrm{bi}}} n_{\mathrm{s}} \tag{S.12}$$

$$\overline{kc_{\mathrm{fi}}} = k_{\mathrm{c,max,f}}\, exp\left[-\frac{\left(E_{\mathrm{c}} - E^{0}_{\mathrm{F,redox,i}} - V_{\mathrm{H}} - \lambda\right)^{2}}{4\lambda K_{\mathrm{B}} T} \right] \tag{S.13}$$

$$\overline{kc_{b\iota}} = k_{\mathrm{c,max,b}}\, exp\left[-\frac{\left(E_{c} - E^{0}_{\mathrm{F,redox,i}} - V_{\mathrm{H}} + \lambda\right)^{2}}{4\lambda K_{\mathrm{B}} T} \right] \tag{S.14}$$

where N_{c} is the density of states of the conduction band, n_{s} is the electron density at the surface, and E_{c} is the conduction band energy level.

Rate equations for OER intermediates at semiconductor sites

The rate equations for fractional coverage of intermediates at a semiconductor site due to charge transfer via both VB and CB can be written as

$$\begin{aligned}\dot{\theta}_{\mathrm{OH}} = {} & K_{\mathrm{vf1}} x_{\mathrm{OH}}\,\theta_{\mathrm{ad}} - K_{\mathrm{vb1}}\theta_{\mathrm{OH}} - K_{\mathrm{vf2}}\theta_{\mathrm{OH}} x_{\mathrm{OH}} + K_{\mathrm{vb2}}\theta_{\mathrm{O}} x_{\mathrm{H_2O}} \\ & + K_{\mathrm{cf1}} x_{\mathrm{OH}}\,\theta_{\mathrm{ad}} - K_{\mathrm{cb1}}\theta_{\mathrm{OH}} - K_{\mathrm{cf2}}\theta_{\mathrm{OH}} x_{\mathrm{OH}} + K_{\mathrm{cb2}}\theta_{\mathrm{O}} x_{\mathrm{H_2O}}\end{aligned} \tag{S.15}$$

$$\begin{aligned}\dot{\theta}_{\mathrm{O}} = {} & K_{\mathrm{vf2}} x_{\mathrm{OH}}\;\theta_{\mathrm{OH}} - K_{\mathrm{vb2}}\theta_{\mathrm{O}} x_{\mathrm{H_2O}} - K_{\mathrm{vf3}}\theta_{\mathrm{O}} x_{\mathrm{OH}} + K_{\mathrm{v}b3}\theta_{\mathrm{OOH}} \\ & + K_{\mathrm{cf2}} x_{\mathrm{OH}}\;\theta_{\mathrm{OH}} - K_{\mathrm{cb2}}\theta_{\mathrm{O}} x_{\mathrm{H_2O}} - K_{\mathrm{cf3}}\theta_{\mathrm{O}} x_{\mathrm{OH}} + K_{\mathrm{cb3}}\theta_{\mathrm{OOH}}\end{aligned} \tag{S.16}$$

$$\begin{aligned}\dot{\theta}_{\mathrm{OOH}} = {} & K_{\mathrm{vf3}}\theta_{\mathrm{O}} x_{\mathrm{OH}} - K_{\mathrm{v}b3}\theta_{\mathrm{OOH}} - K_{\mathrm{v}f4}\theta_{\mathrm{OOH}} x_{\mathrm{OH}} + K_{\mathrm{vb4}}\theta_{\mathrm{O_2}} x_{\mathrm{H_2O}} \\ & + K_{\mathrm{cf3}}\theta_{\mathrm{O}} x_{\mathrm{OH}} - K_{\mathrm{cb3}}\theta_{\mathrm{OOH}} - K_{\mathrm{cf4}}\theta_{\mathrm{OOH}} x_{\mathrm{OH}} + K_{\mathrm{cb4}}\theta_{\mathrm{O_2}} x_{\mathrm{H_2O}}\end{aligned} \tag{S.17}$$

$$\begin{aligned}\dot{\theta}_{\mathrm{O_2}} = {} & K_{\mathrm{vf4}}\theta_{\mathrm{OOH}} x_{\mathrm{OH}} - K_{\mathrm{vb4}}\theta_{\mathrm{O_2}} x_{\mathrm{H_2O}} + K_{\mathrm{cf4}}\theta_{\mathrm{OOH}} x_{\mathrm{OH}} - K_{\mathrm{cb4}}\theta_{\mathrm{O_2}} x_{\mathrm{H_2O}} \\ & - K_{\mathrm{f5}}\theta_{\mathrm{O_2}}\end{aligned} \tag{S.18}$$

$$\theta_{ad} = 1 - \theta_{\mathrm{OH}} - \theta_{O} - \theta_{OOH} - \theta_{O_2} \tag{S.19}$$

where x_{OH} represents the mole fraction of hydroxyl ions and $x_{\mathrm{H_2O}}$ represents the mole fraction of water.

Current density due to charge transfer via VB and CB

The forward and backward current densities for charge transfer via VB (subscript V) and CB (subscript C) are calculated as

$$j_{\mathrm{vf}} = eN_0\left(K_{\mathrm{vf1}}\theta_{\mathrm{ad}} + K_{\mathrm{vf2}}\theta_{\mathrm{OH}} + K_{\mathrm{vf3}}\theta_{\mathrm{O}} + K_{\mathrm{vf4}}\theta_{\mathrm{OOH}}\right)x_{OH} \tag{S.20}$$

$$j_{\mathrm{vb}} = eN_0\left(K_{\mathrm{vb1}}\theta_{\mathrm{OH}} + K_{\mathrm{vb2}}\theta_{\mathrm{O}} x_{\mathrm{H_2O}} + K_{\mathrm{vb3}}\theta_{\mathrm{OOH}} + K_{\mathrm{vb4}}\theta_{\mathrm{O_2}} x_{\mathrm{H_2O}}\right) \tag{S.21}$$

$$j_{\mathrm{v}} = j_{\mathrm{vf}} - j_{\mathrm{vb}} \tag{S.22}$$

$$j_{\mathrm{cf}} = eN_0\left(K_{\mathrm{cf1}}\theta_{\mathrm{ad}} + K_{\mathrm{cf2}}\theta_{\mathrm{OH}} + K_{\mathrm{cf3}}\theta_{\mathrm{O}} + K_{\mathrm{cf4}}\theta_{\mathrm{OOH}}\right)x_{\mathrm{OH}} \tag{S.23}$$

$$j_{\mathrm{c}b} = eN_0\left(K_{\mathrm{cb1}}\theta_{\mathrm{OH}} + K_{\mathrm{cb2}}\theta_{\mathrm{O}} x_{\mathrm{H_2O}} + K_{\mathrm{cb3}}\theta_{\mathrm{OOH}} + K_{\mathrm{cb4}}\theta_{\mathrm{O_2}} x_{\mathrm{H_2O}}\right) \tag{S.24}$$

$$j_{\mathrm{c}} = j_{\mathrm{cf}} - j_{\mathrm{cb}} \tag{S.25}$$

S1.3 Charge transfer via r-SS

Rate constants for charge transfer via r-SS

The surface states which act as recombination centers are called recombining surface states (r-SS). The rate constants for charge transfer via r-SS are calculated as [3]

$$K_{\mathrm{tfi}} = \overline{kt_{\mathrm{fi}}}(1 - f)(N_{\mathrm{T}}/d) \tag{S.26}$$

$$K_{t_{\mathrm{bi}}} = \overline{kt_{\mathrm{bi}}} f(N_{\mathrm{T}}/d) \qquad \text{(S.27)}$$

$$\overline{kt_{\mathrm{fi}}} = k_{\mathrm{t,max,f}} \exp\left[-\frac{\left(E_{\mathrm{T}} - E^0_{\mathrm{F,redox,i}} - V_{\mathrm{H}} - \lambda\right)^2}{4\lambda K_{\mathrm{B}} T}\right] \qquad \text{(S.28)}$$

$$\overline{kt_{\mathrm{bi}}} = k_{\mathrm{t,max,b}} \exp\left[-\frac{\left(E_{\mathrm{T}} - E^0_{\mathrm{F,redox,i}} - V_{\mathrm{H}} + \lambda\right)^2}{4\lambda K_{\mathrm{B}} T}\right] \qquad \text{(S.29)}$$

where N_{T} is the density of states of r-SS, f is the fill factor of r-SS, d is the thickness of the hole accumulation layer, and is used to convert the surface concentration (per cm^2) to volume concentration (per cm^3).[8]

Rate equations for OER intermediates at sites corresponding to r-SS

The rate equations for fractional coverage of intermediates at an r-SS site due to charge transfer via r-SS are calculated as

$$\dot{\theta}T_{\mathrm{OH}} = K_{\mathrm{tf}_1} x_{\mathrm{OH}}\, \theta T_{\mathrm{ad}} - K_{\mathrm{tb}_1} \theta T_{\mathrm{OH}} - K_{\mathrm{tf}_2} \theta T_{\mathrm{OH}} x_{\mathrm{OH}} + K_{\mathrm{tb}_2} \theta T_{\mathrm{O}} x_{\mathrm{H_2O}} \qquad \text{(S.30)}$$

$$\dot{\theta}T_{\mathrm{O}} = K_{\mathrm{tf}_2} x_{\mathrm{OH}}\, \theta T_{\mathrm{OH}} - K_{\mathrm{tb}_2} \theta T_{\mathrm{O}} x_{\mathrm{H_2O}} - K_{\mathrm{tf}_3} \theta T_{\mathrm{O}} x_{\mathrm{OH}} + K_{\mathrm{tb}_3} \theta T_{\mathrm{OOH}} \qquad \text{(S.31)}$$

$$\dot{\theta}T_{\mathrm{OOH}} = K_{\mathrm{tf}_3} \theta T_{\mathrm{O}} x_{\mathrm{OH}} - K_{\mathrm{tb}_3} \theta T_{\mathrm{OOH}} - K_{\mathrm{tf}_4} \theta T_{\mathrm{OOH}} x_{\mathrm{OH}} + K_{\mathrm{tb}_4} \theta T_{\mathrm{O_2}} x_{\mathrm{H_2O}} \qquad \text{(S.32)}$$

$$\dot{\theta}T_{\mathrm{O_2}} = K_{\mathrm{tf}_4} \theta T_{\mathrm{OOH}} x_{\mathrm{OH}} - K_{\mathrm{tb}_4} \theta T_{\mathrm{O_2}} x_{\mathrm{H_2O}} - K_{\mathrm{f5}} \theta T_{\mathrm{O_2}} \qquad \text{(S.33)}$$

$$\theta T_{\mathrm{ad}} = 1 - \theta T_{\mathrm{OH}} - \theta T_{\mathrm{O}} - \theta T_{\mathrm{OOH}} - \theta T_{\mathrm{O_2}} \qquad \text{(S.34)}$$

Current density due to charge transfer via r-SS

The forward and backward current densities for charge transfer via r-SS are calculated as

$$j_{\mathrm{tf}} = eN_{\mathrm{ss}}\left(K_{\mathrm{tf}_1} \theta T_{\mathrm{ad}} + K_{\mathrm{tf}_2} \theta T_{OH} + K_{\mathrm{tf}_3} \theta T_{\mathrm{O}} + K_{\mathrm{tf}_4} \theta T_{\mathrm{OOH}}\right) x_{\mathrm{OH}} \qquad \text{(S.35)}$$

$$j_{\mathrm{tb}} = eN_{\mathrm{ss}}\left(K_{\mathrm{tb}_1} \theta T_{\mathrm{OH}} + K_{\mathrm{tb}_2} \theta T_{\mathrm{O}} x_{\mathrm{H_2O}} + K_{\mathrm{tb}_3} \theta T_{\mathrm{OOH}} + K_{\mathrm{tb}_4} \theta T_{\mathrm{O_2}} x_{\mathrm{H_2O}}\right) \qquad \text{(S.36)}$$

$$j_{\mathrm{t}} = j_{\mathrm{tf}} - j_{\mathrm{tb}} \qquad \text{(S.37)}$$

S1.4 Calculation of the total current density

The total current density is calculated based on Eq. S.20-S.25 and Eq. S.35-S.37 as

$$j = j_{\mathrm{v}} + j_{\mathrm{c}} + j_{\mathrm{t}} \qquad \text{(S.38)}$$

$$j = j_{\mathrm{vf}} + j_{\mathrm{cf}} + j_{\mathrm{tf}} - j_{\mathrm{vb}} - j_{\mathrm{cb}} - j_{\mathrm{tb}} \qquad \text{(S.39)}$$

S1.5 Implementation of IR drop in the model

The potential drop over the series resistance, R_s, depends on the current density in the circuit. The implementation of the potential drop over R_s in the model is shown as a schematic in Figure S1.

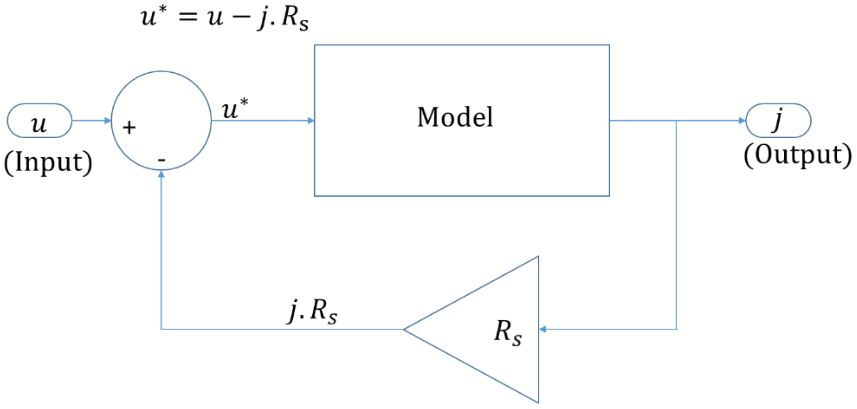

Figure S1 Schematic representation of the implementation of potential drop over the series resistance in the model; u^* represents the input potential to the model after correcting for a potential drop over R_s.

S2. Gibbs free energy and redox potential

The Gibbs free energies for the intermediates steps in OER on hematite are calculated using DFT.[9] Previously, in Zhang et al.[9], we have calculated Gibbs free energies for OER intermediates on hematite surfaces using DFT calculations, assuming a gas-solid interface. The gas-solid model does not account for solvent effects in the calculation of the free energies. In this study, an (implicit) solid-liquid model of the hematite-water interface is used wherein the solvent effects are accounted for by using a continuum solvation model with the dielectric constant of water (ϵ = 78.4) as implemented in VASPsol.[10] The redox potentials of the intermediate steps in OER are calculated using DFT. The spin-polarized DFT+U (U = 4.3 eV) formalism is chosen in order to treat the correlation effects in 3d electrons in hematite.[11] The Perdew–Burke–Ernzerhof (PBE) XC functional [12] and the projected augmented wave (PAW)[13] potentials were used. The molecular geometries were fully optimized with VASPsol when incorporating solvent effects. A 2x2 supercell of hematite (110) is used which is modeled as being antiferromagnetic (net zero spin via the MAGMOM keyword in VASP).[11,14] Zero-point energy correction and entropic contributions to the Gibbs free energy were obtained via Hessian calculation on the optimized geometry.

Table S2 Gibbs free energies calculated for OER intermediate steps on hematite (110) surface.

Parameter	Description	Value
ΔG_1	Gibbs free energy for the step in Eq. (S.2)	1.87 eV
ΔG_2	Gibbs free energy for the step in Eq. (S.3)	1.97 eV
ΔG_3	Gibbs free energy for the step in Eq. (S.4)	0.97 eV
ΔG_4	Gibbs free energy for the step in Eq. (S.5)	0.11 eV

The redox potential corresponding to each intermediate step can be calculated based on the relation between Gibbs free energy and redox potential given by[15]

$$E_{\text{redox,i}} = \frac{\Delta G_i}{nF} \tag{S.40}$$

where n is the number of electrons transferred in a single step (n = 1 for all steps here), F is the Faraday's constant, and $E_{\text{redox,i}}$ is the redox potential of the intermediate step.

S3. Experimental j-V plot for different illumination intensities

Experimental j-V plot for three different illumination intensities replotted from the literature for comparison with the simulations shown in Figure 3 of the main text.[16]

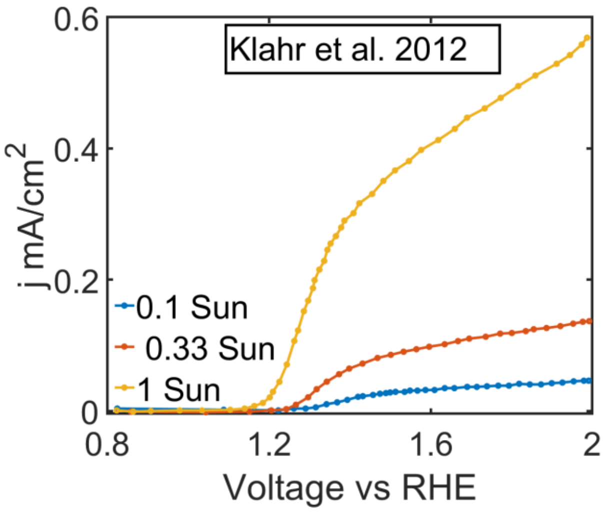

Figure S2 Experimental j-V plots for three different illumination intensities for hematite electrodes replotted from Klahr et al.[16]

S4. Simulated data for R_s = 0

The j-V curves, C_{i-SS} plots, and Mott-Schottky plots are simulated for three different illumination intensities by keeping R_s = 0 as shown in Figure S3. For all the three illumination intensities C_{i-SS} shows peaks around the OER onset potential. However, no deviation in linearity is observed in the Mott-Schottky plot around the potential range of C_{i-SS}. Therefore, the deviation in linearity observed in the Mott-Schottky plot in Figure 6 of the main text cannot be attributed to C_{i-SS}.

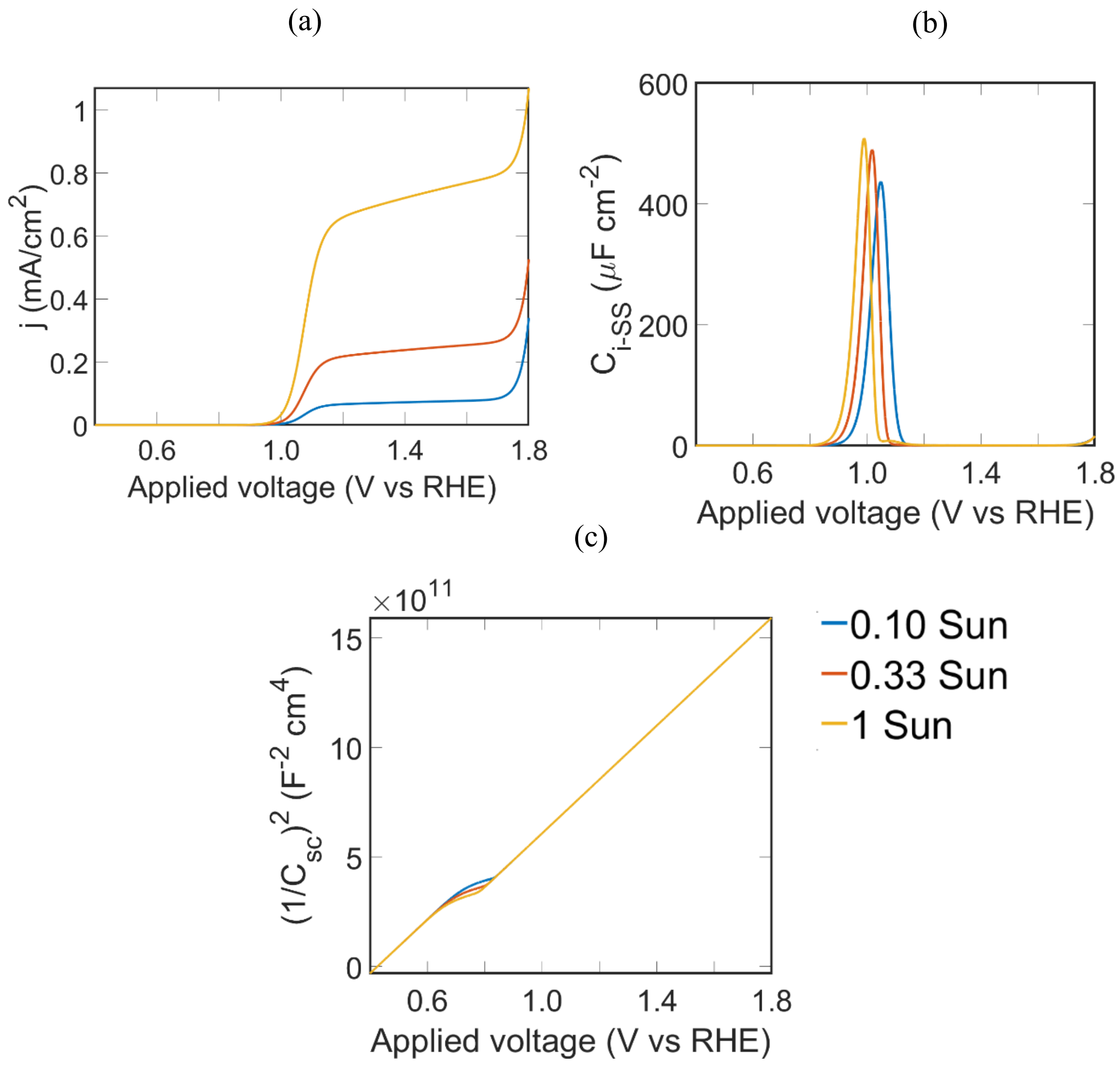
(a)

(b)

(c)

Figure S3 a) j-v plot, b) surface state capacitance $C_{\mathrm{i-SS}}$, and c) Mott-Schottky plot simulated for the case of R_s = 0. The Mott-Schottky plot shows a deviation from linearity before the onset potential which is related to FLP due to r-SS. However, the Mott-Schottky plot shows no deviation in linearity around the potential range of $C_{\mathrm{i-SS}}$.

S5. Coverage dependent Helmholtz capacitance

In the analysis of PEC data, the Helmholtz capacitance is usually assumed to be constant.[16,17] However, it has been reported in the literature that surface adsorption can affect the Helmholtz capacitance.[18] This will result in Helmholtz capacitance (C_{H}) to be potential dependent through the potential dependence of surface coverage. In this section, we look into a scenario in which the Helmholtz capacitance depends on the coverage of surface intermediates and how it affects the PEC data. For simulating the coverage-dependent Helmholtz capacitance, we consider the simplest model of Helmholtz capacitance which is based on a parallel plate capacitor.

The Helmholtz capacitance per unit area (C_{H0}) in this case, is defined as $C_{\mathrm{H0}} = \epsilon * \epsilon_0 / l$, where l is the thickness of the Helmholtz double-layer, ϵ_0 is the permittivity of free space, and ϵ is the relative permittivity of the semiconductor material.[19,20] An approximate value of 100 μF cm^{-2} is obtained for C_{H0} using $l = 3 \cdot 10^{-8}$ cm and $\epsilon = 38$[21] for hematite.

If we assume that the available area of the capacitor reduces due to surface adsorption, the capacitance based on potential can be calculated as $C_{\mathrm{H}} = C_{\mathrm{H0}} * \theta$, where θ is the fraction of free sites on the surface per unit area. We note that this is a simplified assumption. The idea here is to investigate whether a variation in Helmholtz capacitance based on surface coverage will affect the simulated data. Based on this assumption, the j-V plots, $C_{\mathrm{i-SS}}$, and Mott-Schottky plots are simulated for three different illumination intensities as shown in Figure S4. In these simulations, the contribution due to series resistance is eliminated by keeping $R_{\mathrm{s}} = 0$. Figure S4a shows the j-V plots for three different illumination intensities. $C_{\mathrm{i-SS}}$ plots from Figure S4b show peaks around respective OER onset potential. From Figure S4c, there are two points at which the Mott-Schottky plots show a deviation from linearity. The first one at lower potential is due to r-SS as described in the main text. The second deviation from linearity around the onset potential is enlarged and shown in Figure S4d. The potential range of this second deviation coincides with that of the peaks in the $C_{\mathrm{i-SS}}$ plot. In the main text, it is shown that potential drop over R_{s} can lead to a deviation in the Mott-Schottky plot around the onset potential. However, in this case $R_{\mathrm{s}} = 0$ and, hence, the deviation from linearity observed in the Mott-Schottky plot around the onset potential can be attributed to i-SS. Therefore, if the Helmholtz capacitance varies as a function of surface coverage, i-SS can result in FLP.

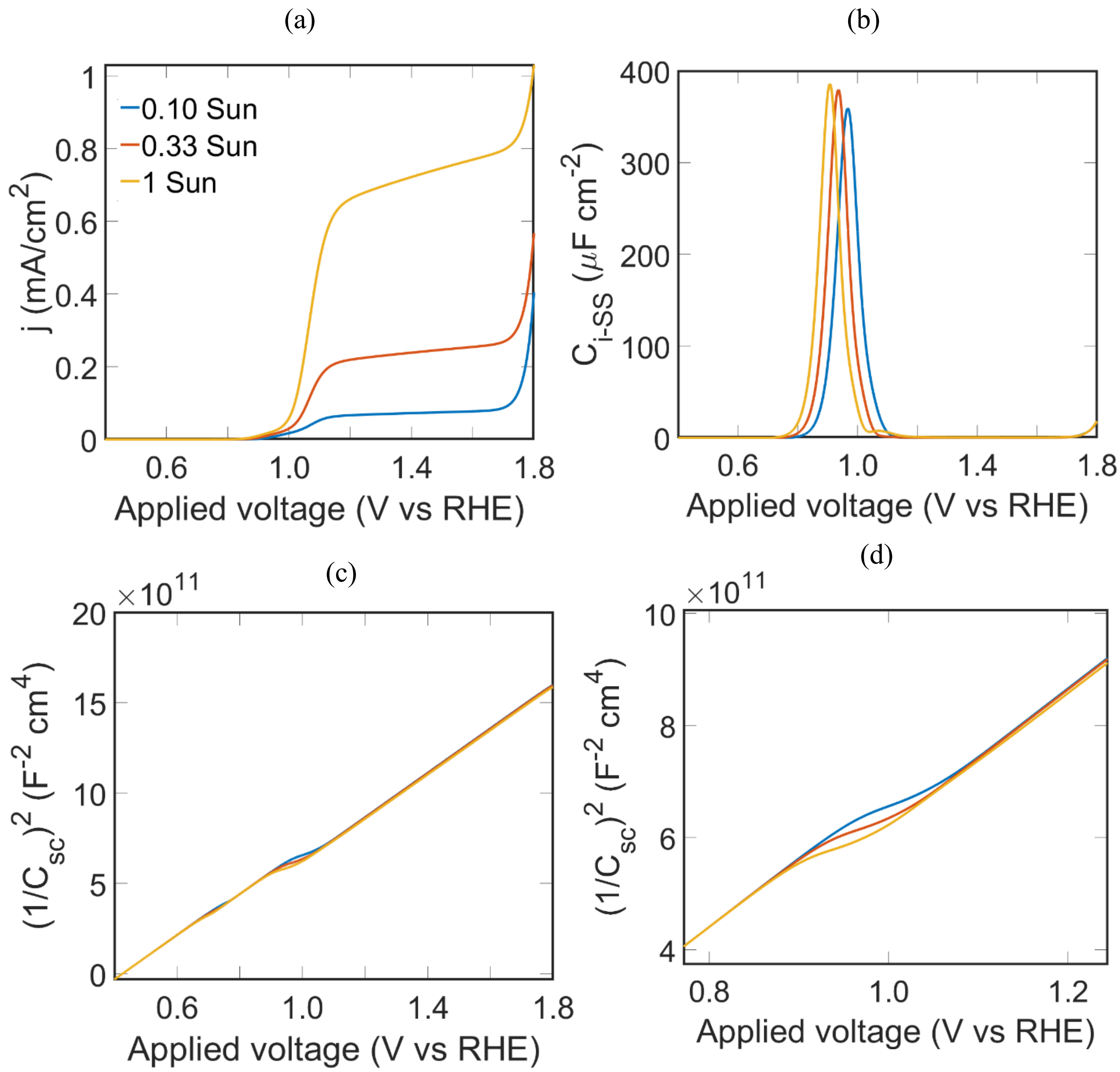

Figure S4 a) j-v plot, b) surface state capacitance $C_{\mathrm{i-SS}}$, c) Mott-Schottky plot simulated for the case of C_H varying as a function of surface coverage. R_s = 0 in all the simulations; d) Enlarged Mott-Schottky plot showing deviation in linearity around the onset potential when the Helmholtz potential is assumed to change with surface coverage, even when R_s = 0.

AUTHOR INFORMATION

[4] Eindhoven University of Technology, Mechanical Engineering, Control Systems Technology, PO Box 513, 5600 MB Eindhoven, The Netherlands.

[5] Delft University of Technology, Process and Energy Department, Faculty of Mechanical, Maritime and Materials Engineering, Leeghwaterstraat 39, 2628CB, Delft, The Netherlands.

References

(1) Hellman, A.; Iandolo, B.; Wickman, B.; Grönbeck, H.; Baltrusaitis, J. Electro-Oxidation of Water on Hematite: Effects of Surface Termination and Oxygen Vacancies Investigated by First-Principles. *Surf. Sci.* **2015**, *640*, 45–49.

(2) Rossmeisl, J.; Qu, Z. W.; Zhu, H.; Kroes, G. J.; Nørskov, J. K. Electrolysis of Water on Oxide Surfaces. *J. Electroanal. Chem.* **2007**, *607*, 83–89.

(3) Rüdiger, M. Charge Transfer Processes at the Semiconductor–Liquid Interface. In *Semiconductor Electrochemistry*; Wiley-Blackwell, 2015; pp 169–266.

(4) Lewis, N. S. Progress in Understanding Electron-Transfer Reactions at Semiconductor/Liquid Interfaces. *J. Phys. Chem. B* **1998**, *102*, 4843–4855.

(5) Heidaripour, A.; Ajami, N.; Miandari, S. Research of Gerischer Model in Transferring Electrons between Energy States of CdS Thin Film and Ferro-Ferric Redox System. **2015**, *3*, 59–64.

(6) Cendula, P.; David Tilley, S.; Gimenez, S.; Bisquert, J.; Schmid, M.; Grätzel, M.; Schumacher, J. O. Calculation of the Energy Band Diagram of a Photoelectrochemical Water Splitting Cell. *J. Phys. Chem. C* **2014**, *118*, 29599–29607.

(7) Hansen, H. A.; Viswanathan, V.; Nørskov, J. K. Unifying Kinetic and Thermodynamic Analysis of 2 e^- and 4 e^- Reduction of Oxygen on Metal Surfaces. *J. Phys. Chem. C* **2014**, *118*, 6706–6718.

(8) Peter, L. M. Energetics and Kinetics of Light-Driven Oxygen Evolution at Semiconductor Electrodes: The Example of Hematite. *J. Solid State Electrochem.* **2013**, *17*, 315–326.

(9) Zhang, X.; Klaver, P.; Van Santen, R.; Van De Sanden, M. C. M.; Bieberle-Hütter, A. Oxygen Evolution at Hematite Surfaces: The Impact of Structure and Oxygen Vacancies on Lowering the Overpotential. *J. Phys. Chem. C* **2016**, *120*, 18201–18208.

(10) http://vaspsol.mse.ufl.edu/.

(11) Liao, P.; Keith, J. A.; Carter, E. A. Water Oxidation on Pure and Doped Hematite (0001) Surfaces: Prediction of Co and Ni as Effective Dopants for Electrocatalysis. *J. Am. Chem. Soc.* **2012**, *134*, 13296–13309.

(12) Perdew, J. P.; Burke, K.; Ernzerhof, M. Generalized Gradient Approximation Made Simple. *Phys. Rev. Lett.* **1996**, *77*, 3865–3868.

(13) Blöchl, P. E. Projector Augmented-Wave Method. *Phys. Rev. B* **1994**, *50*, 17953–17979.

(14) Wang, R. B.; Hellman, A. Hybrid Functional Study of the Electro-Oxidation of Water on Pristine and Defective Hematite (0001). *J. Phys. Chem. C* **2019**, *123*, 2820–2827.

(15) George, K.; van Berkel, M.; Zhang, X.; Sinha, R.; Bieberle-Hütter, A. Impedance Spectra and Surface Coverages Simulated Directly from the Electrochemical Reaction Mechanism: A Nonlinear State-Space Approach. *J. Phys. Chem. C* **2019**, *123*, 9981–9992.

(16) Klahr, B.; Gimenez, S.; Fabregat-Santiago, F.; Hamann, T.; Bisquert, J. Water Oxidation at Hematite Photoelectrodes: The Role of Surface States. *J. Am. Chem. Soc.* **2012**, *134*, 4294–4302.

(17) van de Krol, R.; Grätzel, M. *Photoelectrochemical Hydrogen Production*; Springer: New York, 2012.

(18) Bohra, D.; Chaudhry, J. H.; Burdyny, T.; Pidko, E. A.; Smith, W. A. Modeling the Electrical Double Layer to Understand the Reaction Environment in a CO2 Electrocatalytic System. *Energy Environ. Sci.* **2019**, *12*, 3380–3389.

(19) Bard, A. J.; Bocarsly, A. B.; Fan, F. R. F.; Walton, E. G.; Wrighton, M. S. The Concept of Fermi Level Pinning at Semiconductor/Liquid Junctions. Consequences for Energy Conversion Efficiency and Selection of Useful Solution Redox Couples in Solar Devices. *J. Am. Chem. Soc.* **1980**, *102*, 3671–3677.

(20) Gongadze, E.; Petersen, S.; Beck, U.; Rienen, U. Van. Classical Models of the Interface between an Electrode and an Electrolyte. *Proc. COMSOL Conf. Milan* **2009**, 18–24.

(21) Shavorskiy, A.; Ye, X.; Karslloğlu, O.; Poletayev, A. D.; Hartl, M.; Zegkinoglou, I.; Trotochaud, L.; Nemšák, S.; Schneider, C. M.; Crumlin, E. J.; Axnanda, S.; Liu, Z.; Ross, P. N.; Chueh, W.; Bluhm, H. Direct Mapping of Band Positions in Doped and Undoped Hematite during Photoelectrochemical Water Splitting. *J. Phys. Chem. Lett.* **2017**, *8*, 5579–5586.